







From Orogeny to Rifting: The Role of Inherited Structures During the Formation of the South China Sea

Kai Li^{1,2} , Sascha Brune^{1,3} , Zoltán Erdős¹, Derek Neuharth^{1,4}, Geoffroy Mohn⁵ , and Anne Glerum¹ 

¹GFZ German Research Centre for Geosciences, Potsdam, Germany, ²Institute of Geological Sciences, Freie Universität Berlin, Berlin, Germany, ³Institute of Geosciences, University of Potsdam, Potsdam-Golm, Germany, ⁴Department of Earth and Planetary Sciences, Geological Institute, ETH Zürich, Zürich, Switzerland, ⁵Géosciences et Environnement Cergy (GEC), CY Cergy Paris Université, Neuville sur Oise, France

Key Points:

- We use numerical forward models to assess the impact of orogenic inheritance on rift dynamics
- Thermal inheritance guides the distribution of full or partial thrust fault reactivation
- Continental breakup occurs in regions of previously thick crustal roots

Supporting Information:

Supporting Information may be found in the online version of this article.

Correspondence to:

K. Li,
kai.li@gfz-potsdam.de

Citation:

Li, K., Brune, S., Erdős, Z., Neuharth, D., Mohn, G., & Glerum, A. (2024). From orogeny to rifting: The role of inherited structures during the formation of the South China Sea. *Journal of Geophysical Research: Solid Earth*, 129, e2024JB029006. <https://doi.org/10.1029/2024JB029006>

Received 26 FEB 2024
Accepted 14 NOV 2024

Author Contributions:

Conceptualization: Kai Li, Sascha Brune
Data curation: Kai Li, Geoffroy Mohn
Formal analysis: Kai Li, Zoltán Erdős
Funding acquisition: Kai Li, Sascha Brune
Investigation: Kai Li, Zoltán Erdős, Geoffroy Mohn
Methodology: Kai Li, Sascha Brune, Derek Neuharth, Anne Glerum
Project administration: Sascha Brune
Resources: Sascha Brune
Software: Derek Neuharth, Anne Glerum
Supervision: Sascha Brune
Validation: Sascha Brune, Zoltán Erdős
Visualization: Kai Li
Writing – original draft: Kai Li
Writing – review & editing: Kai Li, Sascha Brune, Zoltán Erdős, Derek Neuharth, Geoffroy Mohn, Anne Glerum

© 2024. The Author(s).

This is an open access article under the terms of the [Creative Commons Attribution License](https://creativecommons.org/licenses/by/4.0/), which permits use, distribution and reproduction in any medium, provided the original work is properly cited.

Abstract Many of the world's rifts and rifted margins have developed within former orogens. The South China Sea (SCS) formed during Cenozoic rifting by utilizing pre-existing orogenic structures, like thrust faults, thickened crust, and corresponding thermal weaknesses. The mechanisms explaining how inherited structures influence the spatiotemporal evolution of a rift remain a topic of on-going research. Here, we explore the impact of orogenic inheritance on rift evolution through a numerical forward model that reproduces geodynamic and landscape evolution processes. By imposing time-dependent phases of shortening and extension, we model rifted margin formation that is consistent with the available geological and geophysical observations of the SCS. Our numerical models allow us to identify thrust faults that are reactivated as normal faults during extensional phases. Not all pre-existing thrust faults, however, undergo full reactivation, as their behavior is influenced by variations in lithospheric strength and the pre-existing structural discontinuities. We further show that inherited orogenic structures compete with each other during extensional reactivation and ultimately govern the location of continental breakup. Our results provide valuable insights into the broader implications of inherited orogenic structures and how they affect subsequent rift system evolution.

Plain Language Summary We investigate the impact of pre-existing geological structures on continental rift evolution. In particular, we focus on the South China Sea (SCS) that was formed within an inhomogeneous mountain belt. Orogenic features preceding rifting, such as thrust faults and thickened crust, have the potential to weaken the lithosphere and to govern subsequent rift tectonics. By using numerical models that include subsequent phases of mountain building and continental rifting, we reproduce geological observations of the SCS rifted margins. We find that inherited orogenic structures play a significant role for localization of faults during the initiation of a rift and ultimately for the location of continental breakup.

1. Introduction

The Wilson cycle, a fundamental concept in plate tectonics, describes a sequence of events involving tectonic divergence and convergence at a plate boundary (Wilson, 1966; Wilson et al., 2019). This cycle involves the fragmentation of a continent, leading to the formation of an oceanic basin. Subsequent stages encompass subduction and closure of the oceanic basin and ultimately the collision between continents, permitting the formation of a new continental landmass. The majority of present-day rifts and rifted margins locate in the region of pre-existing orogenic collision zones (Buitter & Torsvik, 2014). During an orogeny the continental lithosphere experiences significant change via compressional deformation, crustal thickening, and thermal weakening. This orogenic phase is often followed by orogenic collapse, a period of extension and gravitational thinning of the thickened lithosphere (e.g., Dewey, 1988; Jadamec et al., 2007; Molnar & Lyon-Caen, 1988). Consequently, these processes generate weaknesses within the continental lithosphere that play a crucial role in determining the location of extensional deformation (Phillips et al., 2016; Thomas, 2006) and strain localization (Audet & Bürgmann, 2011; Manatschal et al., 2021) during rifting and rifted margin formation (Peron-Pinvidic et al., 2022). Inherited structures are thought to exert a first-order control on the Wilson cycle via multiscale heterogeneities in the thermal state of the lithosphere, compositional variation, and structural complexities (Duretz et al., 2016; Manatschal et al., 2015).

Numerical models of continental extension commonly start with a laterally homogeneous lithosphere to investigate the impact of crustal rheology (Brune, Heine, et al., 2017; Huismans & Beaumont, 2014),

thermal state (Manatschal et al., 2015), yielding mechanisms (Sharples et al., 2015), and extension rate (Naliboff & Buitter, 2015; Tetreault & Buitter, 2018) on the style of rifted margin formation. Other studies have investigated the impact of inherited weakness on rift dynamics (Brune, Corti, & Ranalli, 2017; Corti et al., 2007; Dunbar & Sawyer, 1988; Harry & Sawyer, 1992; Petri et al., 2019; Richter et al., 2021), but did not account for the first-order interaction between tectonics and erosion in mountain belts.

A debate persists around the relative impact of inherited weakness and rift-intrinsic softening processes. For instance, Manatschal et al. (2015) and Jammes and Lavier (2019) proposed that inheritance may exert only limited influence on the location of continental breakup. In contrast, Petersen and Schiffer (2016) investigated the influence of the heterogeneous lithosphere on rift initiation during extension and found that pre-existing orogeny and in particular the existence of fossil slabs plays a crucial role in determining the specific locations where rifting initiates. Furthermore, multiple studies indicate that the process of continental necking may be governed by inherited crustal-scale weaknesses (Huisman & Beaumont, 2007; Wenker & Beaumont, 2018). Comprehensively evaluating the reactivation of faults throughout the Wilson cycle poses a significant challenge, primarily due to overprinting by more recent tectonic events (Camanni & Ye, 2022). Consequently, the specific factors that determine whether inherited weaknesses become reactivated or stay quiescent remain enigmatic. A profound understanding of the significance of inherited structures is essential for precisely modeling and interpreting the dynamics of rift systems (Brune et al., 2023).

In this study, we employ an integrated numerical forward model that combines geodynamic and landscape evolution software (Neuharth et al., 2022b). By systematically altering our velocity boundary conditions across temporal stages, our two-dimensional model accounts for successive phases of continental collision, post-orogenic collapse, continental rifting, and finally continental breakup as observed in the South China Sea (SCS). Our reference model reproduces first-order geological and geophysical observations from the study region and provides insight into the dynamic interaction between mechanical deformation, thermal inheritance and surface processes. In particular, we analyze which processes lead to the full or partial reactivation of thrust faults as well as the final location of continental breakup. To investigate the role of orogenic inherited structures in general, we further present alternative model scenarios that include different shortening velocities, surface erosion rates and crustal strength.

2. Wilson Cycle Tectonics in the South China Sea

The SCS constitutes the northern part of the Sunda Plate, which is bounded by the Eurasian Plate to the north, the Philippine Sea Plate to the east, and the Indo Australian Plate to the south and west (Argus et al., 2011; Bird, 2003; DeMets et al., 2010; Hayes et al., 2018) (Figure 1). The SCS ocean basin opened during the early Oligocene-middle Miocene, between 33 and 15 Myr ago (Briais et al., 1993; Hall, 2002; Li et al., 2014; Tapponnier et al., 1986; Taylor & Hayes, 1980, 1983), creating seafloor magnetic anomalies (light red lines in Figure 1) that confirm the timing of breakup and spreading (Barckhausen et al., 2014). The solid orange line represents the continent-ocean boundary (COB) of the SCS (Figure 1). The region experienced a late Mesozoic phase of shortening and mountain building (before 100 Myr ago) followed by Paleogene extension (around 65 Myr ago) (Holloway, 1982; Li et al., 2014; Savva et al., 2014), which ultimately led to continental breakup in the early Oligocene (Briais et al., 1993; Larsen et al., 2018; Taylor & Hayes, 1983). The SCS is therefore an ideal place to study the effects of inheritance on rifting and serves as a natural laboratory for the Wilson cycle. Here, we focus on the northern SCS rifted margin and use the timing of main tectonic events of this area for our model boundary conditions.

The Yanshanian orogen which predated the formation of the SCS, is a Mesozoic Andean-type orogen that originated from upper-plate compression related to the NW-ward subduction of the Paleo-Pacific Plate (Jahn et al., 1976; Shi & Li, 2012; Taylor & Hayes, 1983; Xu et al., 2016; Ye et al., 2018; Zhou et al., 2006). Granitoids with different ages (green, blue and purple colors in Figure 1) are found in onshore South China (Li & Li, 2007), on Hainan Island, and at the southern Indochina Peninsula (Fan et al., 2022). Pink colors in Figure 1 indicate the distribution of Mesozoic volcanic arcs in the SCS (Li et al., 2018). Mesozoic granitoid-volcanic rock ages in the onshore region of South China show a distinct seaward renewed migration trend (Li & Li, 2007; Zhou et al., 2006; Zhou & Li, 2000) (Figure 1). The distribution of granitoid rocks and Mesozoic volcanic arcs indicates that during the late Cretaceous post-orogenic stage, southeast-ward migration of magmatism and extensional basins in inland South China were associated with the roll-back of the Paleo-Pacific Plate (Li et al., 2020; Li & Li, 2007). The

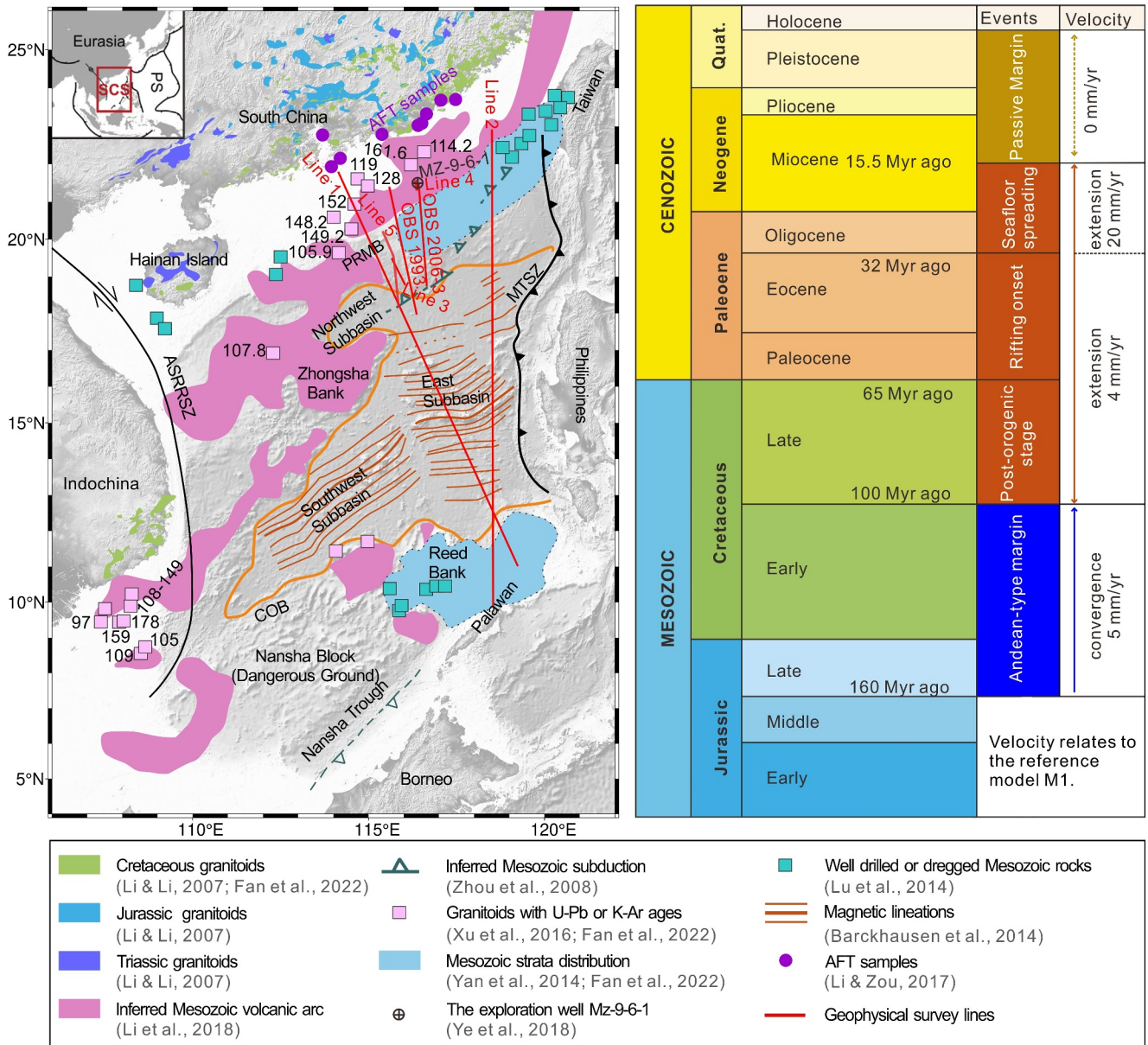


Figure 1. Geological background of the South China Sea (SCS) and locations of data gathered for this study. Line 1 and Line 2 indicate the location of inferred thermal lithosphere-asthenosphere boundary (LAB) depths (Chen et al., 2018). Line 3 (Ye et al., 2018), 4 (Yang et al., 2018) and 5 (Deng et al., 2020) depict seismic profile tracks. Lines OBS 1993 (Yan et al., 2001) and OBS 2006-3 (Wie et al., 2011) represent locations of ocean bottom seismometer (OBS) geophysical experiments. AFT, Apatite-fission-track; ASRRSZ, Ailao Shan-Red River Shear Zone; MTSZ, Manila Trench subduction zone; PRMB, Pearl River Mouth Basin; COB, the continent ocean boundary; PS, Philippine Sea; SCS, South China Sea. The black lines in the overview map in the top-left corner represent plate boundaries. The geological chart shows the tectonic events that occurred in the SCS and the corresponding plate velocity (Brune et al., 2016; Ye et al., 2018) used in reference model M1.

Paleo-Pacific subduction zone was segmented (Zhou et al., 2008) and is marked by green dashed lines with arrows in the northern margin (Figure 1). Furthermore, granitoids from wells in the Pearl River Mouth Basin (PRMB) at the northern margin of the SCS show Zircon U-Pb ages ranging from 161.6 to 101.7 Myr ago (the pink squares in Figure 1), confirming the trend of seaward trench retreat (Fan et al., 2022; Xu et al., 2016). In addition, light blue colors (Figure 1) show the location of major Mesozoic basins in the SCS (Fan et al., 2022; Yan et al., 2014). The MZ-9-6-1 well (Figure 1) was drilled into Mesozoic strata (Ye et al., 2018). The light green squares in Figure 1 show the locations of drilled or dredged Mesozoic rocks (Lu et al., 2014). Thrust faults that accommodated shortening during the Mesozoic were shown to be reactivated during subsequent stretching (Deng et al., 2021; Suo et al., 2019; Ye et al., 2018, 2020). The rifted margin architecture in the northern margin of the SCS is

primarily shaped by the reactivation of these inherited fault systems (Camanni & Ye, 2022). The seismic profile of line 3 (Figure 1) shows the reactivation of inherited thrust faults (Ye et al., 2018). The large-scale kinematic evolution of the region has been captured by plate tectonic reconstructions (Zahirovic et al., 2014). In this modeling study we used a simplified kinematic history that approximates far-field plate motions (Brune et al., 2016) in distinct phases: (a) collision at 5 mm/yr, (b) slow extension at 4 mm/yr, (c) fast extension at 20 mm/yr, and (d) tectonic quiescence.

3. Methods

3.1. ASPECT-FastScape Coupling

We apply a numerical forward modeling approach that includes a two-way coupling strategy (Neuharth et al., 2022b) linking the geodynamic, finite element code ASPECT (Heister et al., 2017; Kronbichler et al., 2012) and the landscape evolution model FastScape (Braun & Willett, 2013; Yuan et al., 2019b). We utilize ASPECT to simulate continental lithospheric convergence as well as extension in a 2D Cartesian domain. This software solves the incompressible conservation equations for momentum, mass, and energy assuming an infinite Prandtl number (Equations 1–3; extended Boussinesq approximation) as well as an advection equation for each compositional field (Equation 4):

$$-\nabla \cdot (2\eta\dot{\epsilon}) + \nabla P = \rho\mathbf{g} \quad (1)$$

$$\nabla \cdot \mathbf{u} = 0 \quad (2)$$

$$\bar{\rho}C_p \left(\frac{\partial T}{\partial t} + \mathbf{u} \cdot \nabla T \right) - \nabla \cdot (k\nabla T) = \bar{\rho}H - \alpha\rho T \mathbf{u} \cdot \mathbf{g} \quad (3)$$

$$\frac{\partial c_i}{\partial t} + \mathbf{u} \cdot \nabla c_i = q_i \quad (4)$$

here, η denotes the effective viscosity, $\dot{\epsilon}$ the strain rate tensor (defined as $\frac{1}{2}(\nabla\mathbf{u} + (\nabla\mathbf{u})^T)$, \mathbf{u} the velocity vector, P the pressure, ρ the density, and \mathbf{g} the gravitational acceleration. Temperature evolves through a combination of radioactive heating, shear heating, and adiabatic heating, whereby $\bar{\rho}$ represents the reference adiabatic density, C_p the specific heat capacity, T the temperature, k the thermal conductivity, H the radiogenic heating rate, and α the thermal expansivity. Equation 4 represents the advection equation for each compositional field c_i , taking into account a respective non-zero source term q_i for fields that track the plastic or viscous strain.

The temperature dependence of the densities is given as in Equation 5, where ρ_0 is the reference density and T_0 is the adiabatic reference temperature.

$$\rho = \rho_0 (1 - \alpha(T - T_0)) \quad (5)$$

We employ a nonlinear visco-plastic rheology (Glerum et al., 2018). For the viscous regime, we use a composite of the dislocation (dis) and diffusion (diff) creep viscosities. The effective creep viscosity η_{eff} for each mechanism is computed by Equation 6:

$$\eta_{eff}^{diff|dis} = \frac{1}{2} A_{diff|dis}^{-1} d_{diff|dis}^{-1} a^m \dot{\epsilon}_e^{\frac{1-m}{n}} \exp\left(\frac{(E_{diff|dis} + PV_{diff|dis})}{nRT}\right) \quad (6)$$

here A is the prefactor, $\dot{\epsilon}_e$ the effective deviatoric strain rate (defined as $\sqrt{\frac{1}{2}\dot{\epsilon}'_{ij}\dot{\epsilon}'_{ij}}$), d the grain size, E the activation energy, P the pressure, V the activation volume, R the gas constant, and n the stress exponent. For diffusion, when $n = 1$, the equation becomes independent of strain rate. In the case of dislocation creep, the grain size exponent m vanishes, resulting in dislocation creep being independent of grain size. The composition-dependent values for A , E , V , and n are specified in Table S1 in Supporting Information S1.

In the plastic regime, when the viscous stresses exceed the yield stress, we use the Drucker-Prager yield criterion. The effective plastic viscosity is given by Equation 7, where C is the cohesion and ϕ is the angle of internal friction:

$$\eta_{eff}^{pl} = \frac{C \cos(\phi) + P \sin(\phi)}{2\dot{\epsilon}_e} \quad (7)$$

ASPECT is coupled to the surface process modeling code FastScape. This software simulates several key physical processes that play a role in shaping the topography of the Earth's surface, including fluvial erosion (which is governed by the stream-power law), hillslope and marine diffusion, and horizontal advection (Braun & Willett, 2013; Yuan et al., 2019a, 2019b).

Equation 8 represents processes in the continental domain:

$$\frac{dh}{dt} = U - K_f A^m S^n + \frac{G}{A} \int_A \left(U - \frac{dh}{dt} \right) dA + K_c \nabla^2 h + v \cdot \nabla h \quad (h \geq h_{sea}) \quad (8)$$

accounting for the topographic elevation h , the uplift rate U , the bedrock erodibility K_f , the drainage area A , the slope S , the drainage area exponent m , the slope exponent n , the deposition coefficient G , the continental diffusion coefficient K_c , the lateral velocity v , and the sea level h_{sea} .

Equation 9 represents marine processes:

$$\frac{dh}{dt} = U + K_m \nabla^2 h + Q_s + v \cdot \nabla h + Q_0 \quad (h < h_{sea}) \quad (9)$$

here K_m is the marine diffusion coefficient, Q_s the sediment flux, and Q_0 the oceanic background sedimentation rate. ASPECT operates in 2D along a vertical XZ -plane with far-field plate motions imposed along the X -direction, whereas FastScape functions in 2D in a horizontal XY -plane located at the Earth's surface (Figure 2a). To accomplish the two-way coupling, ASPECT's velocities are duplicated along the Y -direction and provide an X -dependent uplift rate U as input for FastScape. FastScape modifies the surface topography and returns it to ASPECT by averaging topography along the Y -direction, such that ASPECT's vertical mesh velocities can be updated. This way, topographic changes and vertical motions are effectively exchanged and synchronized between both codes (Neuharth et al., 2022a, 2022b).

3.2. Experimental Setup

The initial geometry of our reference model M1 is designed to reproduce the state of the proto-southeast Asian lithosphere prior to the formation of the Andean-type orogen (Holloway, 1982; Morley, 2012; Taylor & Hayes, 1983) that subsequently rifted apart to create the present-day SCS. Lateral boundary conditions reproduce the main phases of shortening, extension, and tectonic quiescence that shaped the SCS region from Jurassic to present-day as shown in Figure 1. In the following, we first describe the setup of our reference model M1 in detail and then briefly address the setup of alternative models M2 to M8.

3.2.1. Model Geometry and Initial Conditions

The 2D model domain spans 700 km horizontally and 200 km vertically and is initialized with four compositional layers (Figure 2): a 25 km thick upper crust and a 15 km thick lower crust overlying an 80 km thick mantle lithosphere, and an 80 km thick asthenosphere. The initial compositional lithosphere-asthenosphere boundary (LAB) hence locates at a depth of 120 km. To initiate the onset of continental orogeny in the model center, we introduce a lithospheric weakness by increasing the thickness of the central upper crust to 26 km and that of the lower crust to 16 km, resulting in a total crustal thickness of 42 km using a Gaussian distribution with a half width of 25 km around the model center. We equilibrate lithospheric temperatures before model start using a 1D analytical solution. The thicker crust leads to a slightly warmer steady-state lithosphere and to about 170 m of positive isostatic topography at the center of the model domain.

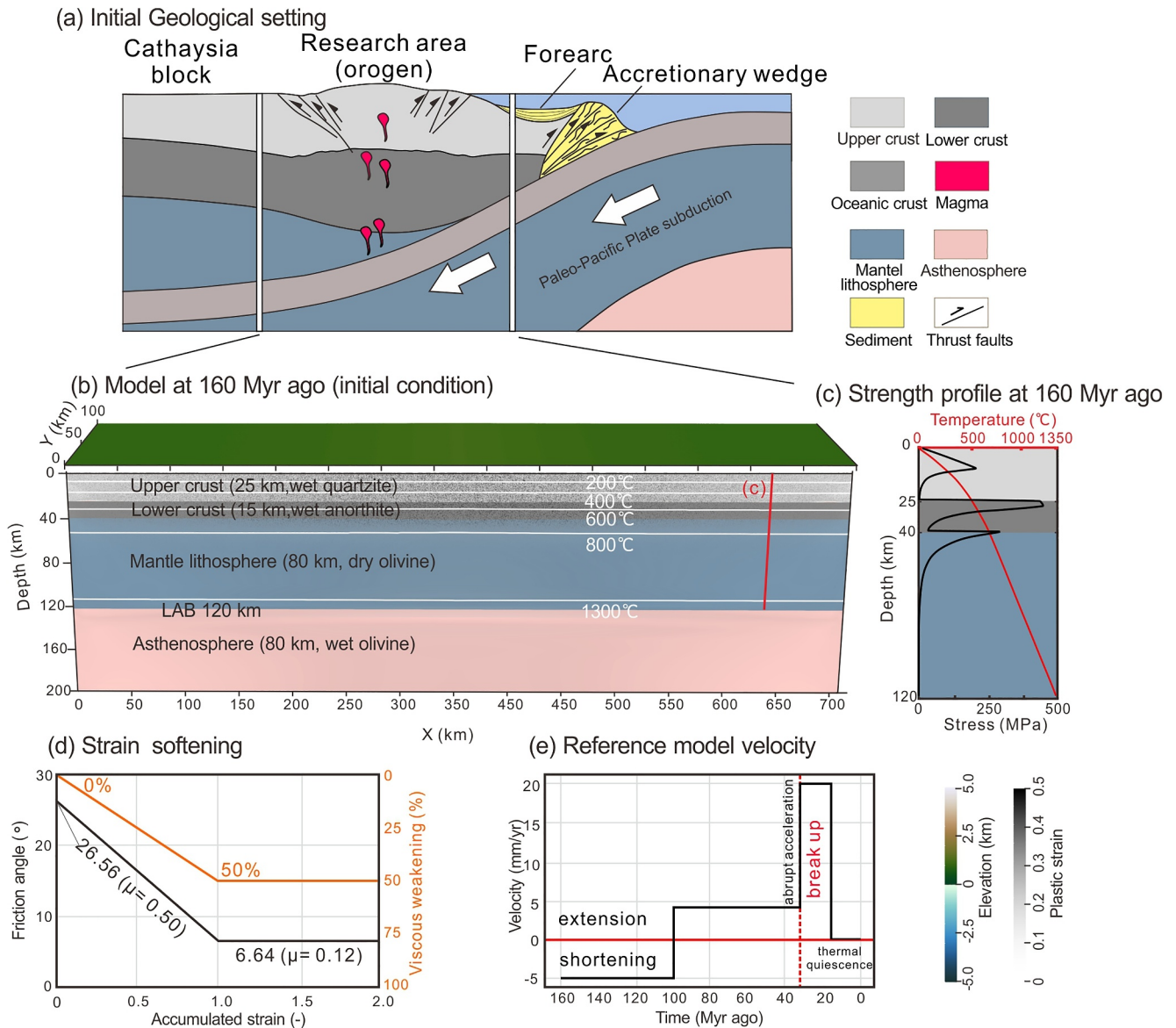


Figure 2. (a) Conceptual geological setting of the study region in the Mesozoic, including the subduction of the paleo-Pacific Plate, crustal thickening, thrust faulting, orogeny, and magmatism. Our model domain is restricted to the orogenic area. (b) Initial model configuration. Shown are the surface process model (FastScape) at the top and the 2D tectonic model (ASPECT) at the bottom. The central areas of the ASPECT model exhibit random initial plastic strain, which has a value defined by a Gaussian distribution around the horizontal center of the domain with an amplitude of 0.5. The white lines indicate temperature contours. A traction boundary condition allowing for in- and outflow of material is applied at the base of the model to ensure isostasy and mass conservation (see Section 3.2.3). (c) Initial strength profile (in black) and temperature profile (in red) for the reference model M1. The strength profile shows the second invariant of the deviatoric stress tensor. (d) Plastic and viscous weakening is a piece-wise linear function of accumulated plastic and viscous strain, respectively. (e) Variations in the velocity boundary conditions throughout the model evolution.

The model is characterized by a mesh resolution varying between 156 m and 10 km, based on the temperature and spatially prescribed refinement steps. The highest resolution of 156 m is reserved for depths of 0–30 km. In areas of greater depth, the resolution has a maximum value of 312 m in regions where temperatures remain below 927°C. Outside these domains, the resolution is 10 km. As a result, areas affected by faulting remain significantly refined. To ensure an accurate representation of the solution, the mesh is updated every five timesteps. In the central regions of the reference model M1, particles are incorporated to trace pressure-temperature-time paths. This setting is applied only to M1. These passive particles are initially uniformly distributed within a 500 km (100–600 km in the x -direction) wide box located in the upper 30 km of the domain. FastScape is executed on a mesh with a resolution of 312 m, which remains uniform throughout the entire simulation.

3.2.2. Material Properties and Weakening Mechanisms

Our model lithosphere consists of a wet quartzite upper crust (Gleason & Tullis, 1995; Rutter & Brodie, 2004), wet anorthite lower crust (Rybacki et al., 2006), and dry olivine mantle lithosphere (Hirth & Kohlstedt, 2003). The asthenosphere consists of wet olivine (Hirth & Kohlstedt, 2003). In the SCS, the rifted margins are wide, attributed to elevated temperatures and reduced lithospheric strength during the rifting process (e.g., Brune, Heine, et al., 2017; Clerc et al., 2018; Franke et al., 2014). Additionally, heat production measurements show relatively high values within the sedimentary layers and upper crust (Hu et al., 2020), ranging from 1.65 to 2.0 (W m^{-3}). In particular, we consider a relatively high radiogenic heat productivity of 1.4×10^{-6} (W m^{-3}) and 1.65×10^{-6} (W m^{-3}) for the modeled sediments and upper crust, respectively (Beaumont et al., 2004; Hasterok et al., 2018). The parameters associated with the properties of all layers can be found in Table S1 in Supporting Information S1 within the Supporting Information.

To enable localization of faults and shear zones, we use strain-dependent weakening for (a) brittle layers (Persaud et al., 2017; Salazar-Mora et al., 2018) and (b) ductile layers (Döhmann et al., 2019; Gerbi et al., 2010; Pérez-Gussinyé et al., 2020). The reference model M1 incorporates plastic weakening through a linear reduction of the friction angle by 75%. This reduces the initial angle of 26.56° to a final angle of 6.64° (corresponding to friction coefficients of 0.5 and 0.12, respectively) as a function of accumulated plastic strain within the interval of 0–1 (Figure 2d). Viscous weakening is included by a 50% reduction in the effective viscosity (Table S1 in Supporting Information S1) within the accumulated viscous strain range from 0 to 1 (Figure 2d). Note that plastic strain weakening is mesh-dependent and the arbitrarily defined weakening interval of 0–1 is similar to that used in other thermo-mechanical numerical modeling studies (e.g., Neuharth et al., 2022b; Salazar-Mora et al., 2018). The asthenosphere is excluded from viscous weakening processes. Furthermore, accumulated strain is initialized via random noise (with a value between 0.0 and 0.5; Figure 2b) to consistently break the initial symmetry and to reflect the non-homogeneity of natural rocks (Heckenbach et al., 2021; Jammes & Lavier, 2019; Naliboff et al., 2020; Richter et al., 2021). The width of the Gaussian distribution of the strain noise amplitude is horizontally defined through the standard deviation of $2\sigma = 600$ km and the noise is smoothed out at a depth of 50 km (Figure 2b).

3.2.3. Boundary Conditions

Models M1 to M7 are subjected to far-field kinematics similar to that of the SCS, with distinct phases of deformation: an initial phase of shortening, a subsequent phase of extension (initially slow then fast), and a final phase of tectonic quiescence (Figure 1). In addition, model M8, which involves the same initial conditions as the reference model M1, excludes the shortening phase. It directly starts with a period of slow extension, followed by rapid extension, and culminates in a phase of tectonic quiescence (Figure S1 in Supporting Information S1). In all models, the extensional and/or shortening phases are prescribed through a constant material out- or inflow at the left and right boundaries. To achieve mass balance over the model domain, traction boundary conditions are applied to the bottom boundary (Figure 2b): the boundary-normal traction component is set to the lithostatic pressure at the bottom computed by integrating the density along a vertical transect at $x = 5$ km using the initial conditions for temperature and composition. At the same time, the boundary-parallel component of traction is set to zero. This boundary condition allows for the specific in- or outflow of material through the boundary to conserve mass and to ensure that surface points of undeformed lithosphere remain at almost constant elevation throughout the model run.

The reference model M1 initially undergoes a period of shortening between 160 and 100 Myr ago, characterized by an inflow velocity of 5 mm/yr (Figure 2e). The subsequent extension starts after 60 Myr of model time and is characterized by an outflow velocity of 4 mm/yr. An abrupt acceleration of the extensional velocity (to 20 mm/yr) occurs 32 Myr ago. The final stage of tectonic quiescence lasts from 15 Myr ago to the present, with boundary velocities close to zero. The landscape evolution code FastScape is coupled to the top of the tectonic model, introducing material transport via surface processes such as river incision, hillslope diffusion, and sedimentation (see Section 3.1).

Thermal boundary conditions are set as follows. The top boundary is fixed to a temperature of 0°C while the bottom temperature of $1,380^\circ\text{C}$ is computed based on the initial adiabat of the asthenosphere. No heat flow is permitted across the side boundaries of the tectonic model.

Table 1
Key Parameters of Reference Model M1 and Alternative Models M2 to M8

Model	Upper crustal thickness (km)	Lower crustal thickness (km)	Shortening velocity (mm/yr)	Erodibility K_f ($m^{0.2}/yr$)
M1	25	15	5	10^{-5}
M2	25	15	2.5	10^{-5}
M3	25	15	10	10^{-5}
M4	25	15	5	10^{-4}
M5	25	15	5	10^{-6}
M6	23	17	5	10^{-5}
M7	27	13	5	10^{-5}
M8	25	15	No shortening	10^{-5}

Note. Values in bold font indicate the difference with respect to the reference model.

3.2.4. Alternative Model Runs

In addition to our reference model M1, we present alternative models M2 to M7 where we varied three key parameters: the shortening velocity, erosion rate, and initial crustal thickness (Table 1). These parameters exert a distinct control on the model results and are difficult to constrain from observational data. Finally, model M8 has the same basic setup as that of model M1, but there is no initial phase of shortening, and instead the experiment starts straight away with a phase of slow extension. The relevant codes are available at our Zenodo repository (Li, 2024a).

3.3. Model Limitations

Our models are designed to isolate the first-order effects of orogenic inheritance on a subsequent rift phase. We capture first-order processes like the thermal evolution and its transient effects on rheology as well as the interaction between surface processes and tectonics. In comparison to nature, however, our models require four major simplifications: (a) Our simulations adopt a simplified 2D approach for the tectonic model component. We therefore cannot address three-dimensional effects related to along-strike structural changes or rift propagation. (b) We do not explicitly model the dynamics of the subduction system during the initial mountain building phase. Since orogenesis is dominated by lithospheric shortening, we have chosen to focus primarily on this process (Figure 2a) and neglect the impact of slab dynamics, slab break-off or subduction-related delamination which might modulate stresses and topography during mountain building. (c) We do not account for partial melting and melt migration. There are hence no plutonic intrusions during the orogenic phase and no lithospheric weakening during the rifting phase. This also means that our models do not account for the formation of new oceanic crust and depleted mantle. We therefore define breakup as the moment where the continental lithosphere is fully separated. (d) It is also important to note that, although we impose a random initial field of heterogeneities, we do not account for larger-scale pre-existing weaknesses that could be inherited from previous tectonic structures before orogenic times. Despite these simplifications, our models reproduce first-order geological data from the SCS. We are accordingly confident that our numerical experiments offer valuable insights on the influence of inherited structures on the tectonic evolution of the region.

4. Results

We first describe the temporal evolution of our reference model M1, which encompasses a sequence of geological events, starting with overriding plate shortening, followed by post-orogenic collapse, continental rifting, and ultimately continental breakup. We then argue that M1 reproduces the first-order evolution of the SCS region by comparing various aspects of the model with key observations and geological data from the study region. Finally, we describe alternative model scenarios and their relevance for understanding key tectonic processes during the Wilson cycle.

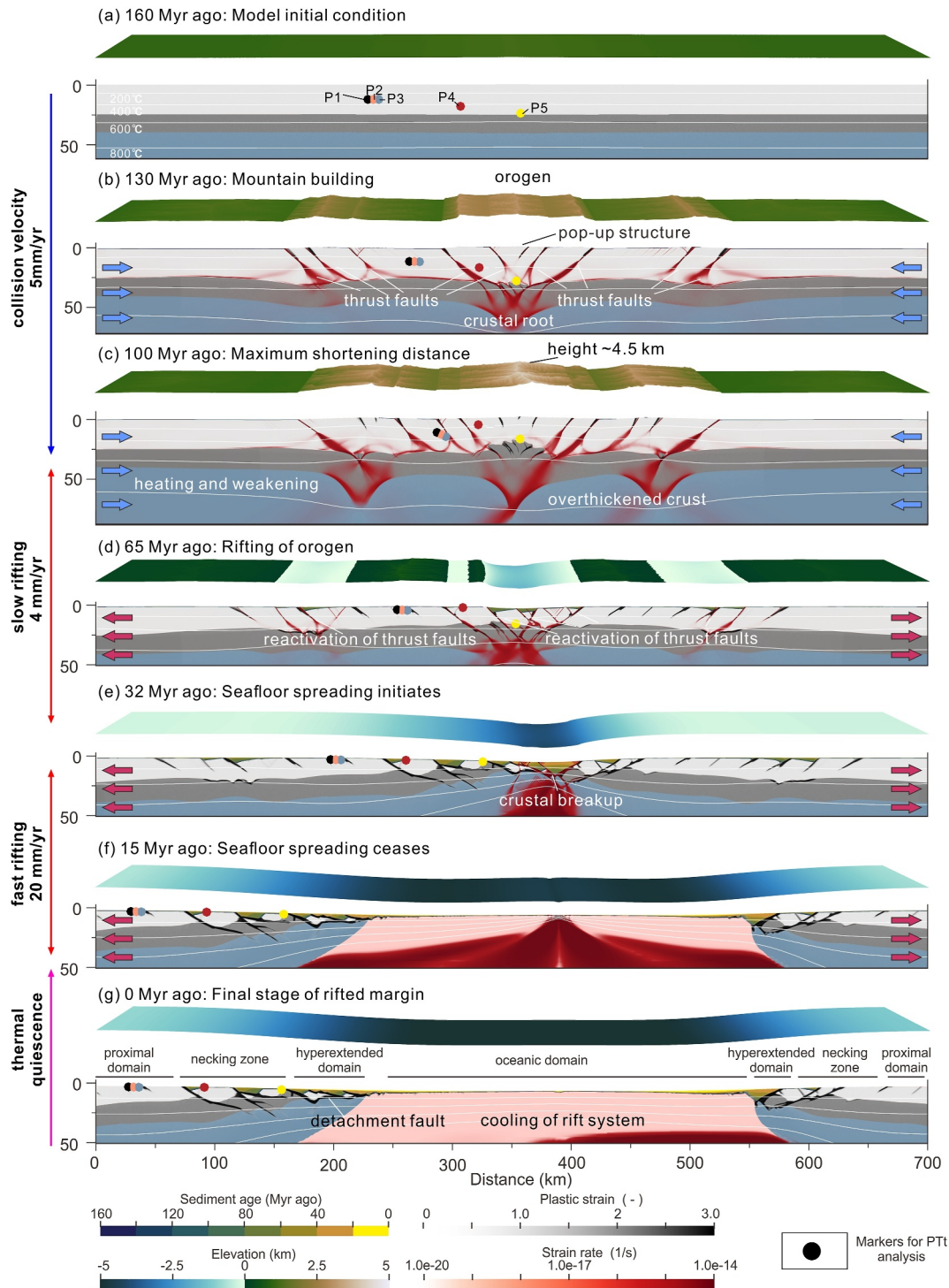


Figure 3. Evolution of the reference model (M1) representing the history of the South China Sea. (a) The model's initial geometry before shortening, with particles labeled P1 to P5 used for tracking the P-T-t path. (b) Orogenic structure after 30 Myr of shortening. (c) Final orogen structure after 300 km of convergence; the maximum elevation reached is approximately 4.5 km. (d) Orogenic rifting with reactivation of thrust faults and formation of sedimentary basins. (e) Continental breakup and the commencement of seafloor spreading 32 Myr ago. (f) Halt of seafloor spreading 15 Myr ago. (g) Final rifted margin structure following a 15 Myr phase of tectonic quiescence. The arrows indicate boundary velocities (e.g., blue for convergence, red for extension). Accumulated plastic strain is shown in black shades, representing brittle faults. Strain rate is depicted in red. White lines contour temperature at 200, 400, 600, and 800°C. Elevation is taken from the FastScape model. See text for further details and Movies S1 and S2 for model evolution. The blue arrows on the left and right sides indicate the shortening phase and the red arrows show the extension phase.

4.1. Evolution of the Numerical Reference Model M1

4.1.1. Structural Evolution

In the reference model M1, mountain building initiates via two groups of oppositely dipping thrust faults in the model center (Figure 3). At 130 Myr ago, these thrust faults are located in the uppermost brittle part of the crust, with only two rooting in the lower crust, and they are accompanied by progressive crustal stacking on either side of the mountain range (Figure 3b). The gradual thickening of the crust, together with internal radiogenic heating and surface erosion, collectively lead to a shallowing of crustal isotherms (Figure 3c). Three crustal blocks located between prominent conjugated thrust faults experience uplift, resulting in the formation of a pop-up structure within the central domain.

As convergence continues, deformation remains concentrated near the principal boundary thrusts. Movement along these thrust faults and crustal thickening beneath uplifted areas mainly accommodate the ongoing shortening (Figure 3c). Within the central crustal root, lower crustal flow effectively accommodates deformation, operating at significantly increased strain rates (Figure 3c). The orogenic peak is reached 100 Myr ago, after 60 Myr of convergence resulting in 300 km of shortening and a maximum crustal thickness of 80 km. Fourteen major thrust faults can be identified, with 50% dipping to the left and 50% to the right, resulting in symmetric double-vergent orogenic structures. The thrust faults are distributed over an area of up to 350 km and spaced 20–50 km apart. Within the center of the orogen, elevated areas reach heights of 4.5 km.

At 100 Myr ago, switching the lateral boundary velocity from inflow to outflow results in a transition of the overall stress field from compressional to tensional. The reversal causes the collapse of the orogen, reactivation of former thrusts as normal faults (Figure 7), and thinning of the previously thickened crust of the orogen. The high-topography central mountain domain collapses first (Movie S1a). As a result, the original mountain terrain sinks and forms a central rift (Figure 3d). At 96 Myr ago, after roughly 16 km of extension, most of the inherited thrust faults are efficiently reused, completely modifying the initial orogenic structures. The crust in the over-thickened crustal rooted regions thins gradually to less than 40 km (Figure 3d). Consequently, isostatic subsidence leads to a lowering of the topography and ultimately permits marine incursion. After 140 km of extension, the continuous normal faulting creates the accommodation space for sediments sourced from mountain erosion, forming sedimentary grabens and half-grabens (Figure 3d).

After approximately 350 km of continental extension, faults are widely distributed over a span of 600 km (Figure 3e). Deformation within the mantle lithosphere localizes into a distinct necking zone, accompanied by the upwelling of the asthenosphere (Figure 3e). Meanwhile, rotation of upper crustal blocks leads to a continuous decrease in fault dip angles. From 32 Myr ago onward, the entire model domain is situated below sea level, with the rifting center at a shallow water depth of around 2 km. Close to the rift center, slip along reactivated thrust faults intensifies (Figure 7d), tilting sedimentary layers and creating new accommodation space for sedimentary units (Figure 3e).

The rapid rifting phase begins 32 Myr ago shortly prior to the inception of continental breakup and at 15 Myr ago seafloor spreading ceases. The conjugate continental margins display distinct differences in width, geometry, and the distribution of basins. The left margin is approximately 360 km in width (including the parts of the margin that have been advected out of the model domain), and features 7 sedimentary basins. The right margin is narrower, measuring 280 km, and develops 2 basins. In the hyperextended domain of both sides, lower crustal rocks are exhumed to depths of less than 10 km (Figure 3f). At the left rifted margin in particular, displacement along the detachment fault's footwall exposes the lower crust to the surface, resulting in a 50 km wide stretch where lower crust is juxtaposed to sediments (Figure 3f). The final dip angle of the detachment fault is approximately 10°, which is caused by the ductile flow of the lower crust and the footwall rotation of reactivated thrust faults.

Following the latest phase of fast extension, a 15 Myr period of tectonic quiescence occurs. During this final phase, the lithosphere gradually cools, and geothermal gradients decrease. Sediments continue to accumulate within the oceanic basins along the rifted margins in undisturbed sub-horizontal layers (Figure 3g).

4.1.2. Pressure-Temperature-Time (P-T-t) Paths

We explore the temporal model evolution through analysis of pressure-temperature-time (P-T-t)-paths extracted from M1. This analysis reveals close similarities with the thermo-tectonic history of the northern SCS (Figure 4a).

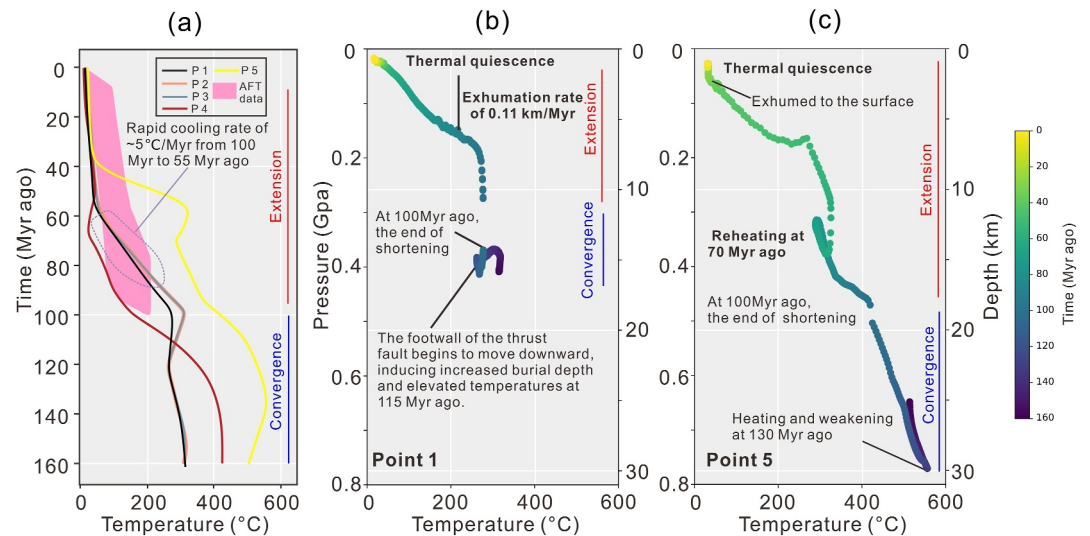


Figure 4. (a) Time-temperature paths derived from apatite fission track (AFT) thermochronology data and extracted from our reference model M1 from convergence to extension. Pink areas represent well-fitted AFT thermochronology data (Li & Zou, 2017) collected from the NE South China Sea coastal region (see Figure 1 for location). Points 1 to 5, which are in different domains of the rifted margin (locations in Figure 3), are selected from M1. The cooling rate of M1 is approximately $5^{\circ}\text{C}/\text{Myr}$ between 100 and 55 Myr ago, which aligns with the AFT data. (b) The pressure-temperature-time (P-T-t) paths of Point 1. It experiences minor heating and weakening around 115 Myr ago. There is a rapid exhumation at this point as the model boundary reverses from inflow to outflow at 100 Myr ago. Point 1, located in the footwall of reactivated faults, exhibits an exhumation rate of $0.11\text{ km}/\text{Myr}$ between 94 and 60 Myr ago (for additional information, refer to Movie S2b). (c) The P-T-t path of Point 5. It experiences heating and weakening around 130 Myr ago. Additionally, another reheating event occurs around 70 Myr ago due to its location in the hanging wall sloping downwards, leading to an increase in burial depth and pressure (for more details, refer to Movie S2c).

The pink shaded area in Figure 4a shows extensive exhumation of the coastal region of NE SCS since 100 Myr ago based on apatite-fission-track (apatite fission track (AFT)) data (see Figure 1 for sample locations). The lines depict the time-temperature paths of the points within the reference model M1. Points within the proximal domain (such as Points 1, 2, and three in Figures 3g and 6a) are consistent with time-temperature results calculated from the AFT ages, showing a cooling rate of approximately $5^{\circ}\text{C}/\text{Myr}$ between 100 and 55 Myr ago. In addition, estimates of AFT data for Late Cretaceous coastal cooling in the northern SCS range from 3 to $8^{\circ}\text{C}/\text{Myr}$ (Li & Zou, 2017; Shi et al., 2022).

Figures 4b and 4c describe the P-T-t evolution of two representative Points 1 and 5 located in the proximal and distal margins, respectively. At 115 Myr ago, toward the end of the shortening phase, Point 1 is located in the footwall of a thrust fault and moves downwards causing increased ambient pressure (Figure 6b). During extension, Point 1 gradually moves toward the surface. Our analysis indicates that between 94 and 60 Myr ago, Point 1 experiences an exhumation from around 6.6 – 1.6 km depth (pressures of 0.17 and 0.04 GPa , respectively, Figure 4b). The corresponding exhumation rate of $0.11\text{ km}/\text{Myr}$ agrees with the previously computed proximal margin exhumation rate of $0.12\text{ km}/\text{Myr}$ (Li & Zou, 2017) during the same time window. Point 5 initially located in the central model domain at the base of the upper crust (Figure 3) experiences the build-up of the central orogen, its collapse and finally exhumation at the distal margin. The exhumation and cooling history of Point 5 is intersected by two stages of reheating (Figure 4c). The first stage takes place during the shortening period, approximately 130 Myr ago. Mountain building and associated increase of radiogenic heat production results in a temperature rise of around 70°C . During the extension stage at around 70 Myr ago, Point 5 experiences a second reheating event. Located on the hanging wall of an inherited thrust fault, the point experiences down-ward motion and burial due to inverted fault reactivation (Figure 3d, Movie S2), resulting in an increased depth from 12 to 15 km . At 40 Myr ago, Point 5 is exhumed to the surface along major normal faults accommodating the exhumation of the deeper parts of the crust.

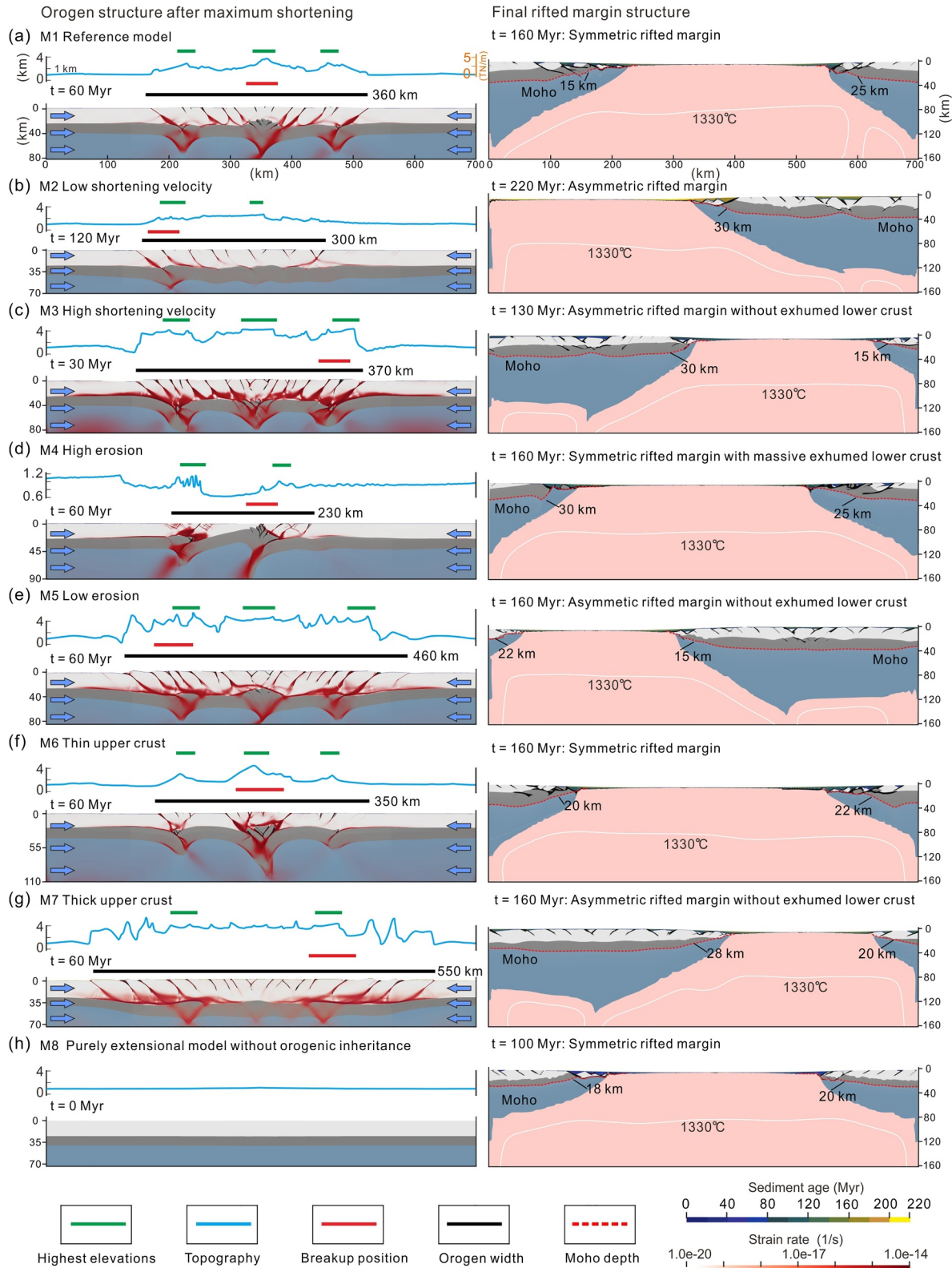


Figure 5.

4.2. Alternative Model Scenarios

Based on the reference model (M1; Figure 3), a series of complementary experiments (Figure 5) were carried out to explore the effects of different collision velocities (models M2 and M3), surface processes (models M4 and M5), and lithosphere rheology (models M6 and M7) on gravitational potential energy (GPE), mountain belt morphology, and the subsequent rift evolution. Key parameters of each model are listed in Table 1, while all other parameters remain identical to M1. We further investigate the differences between models M8 and M1 by comparing their responses to the presence and absence of orogenic inheritance.

4.2.1. The Effect of Collision Velocities: M2 and M3

In models M2 and M3, we investigate the impact of collision velocity. In M2, characterized by a slower convergence velocity (2.5 mm/yr), we observe concentrated deformation along thrust faults in the upper crust, while the lower crust exhibits a more diffuse pattern (Figure 5b). This results in the development of 11 thrust faults in the upper crust, creating several distinct pop-up structures, and a narrower mountain belt spanning about 300 km. The elevation is lower than in M1, measuring less than 2.5 km because of the longer time frame that allows for a higher total erosion. Crustal thickness reaches approximately 55 km, and the Moho exhibits a flatter shape compared to the other models. The rifted margin on the right of Figure 5b displays strong asymmetry due to continental breakup occurring on the left of the orogenic belt, where the crustal root developed with high topographic gradients developed during the orogenic phase.

Conversely, in model M3, which is marked by a higher shortening rate of 10 mm/yr, the width and height of the mountain ranges are greater (Figure 5c). The rapid convergence produces three distinct crustal roots with up to 80 km of crustal thickness and a total of 20 thrust faults. After shortening of 300 km, the mountain range width is around 370 km, with the highest elevation of about 4.2 km. The rifted margin on the right of Figure 5c shows an asymmetric structure due to crustal rupture occurring where the rightmost orogenic crustal root was located.

4.2.2. The Effect of Erosion: Model M4 and M5

Models M4 and M5 have the same fundamental configuration as the reference model M1, but are submitted to different erosional efficiencies (Table 1). In the case of more efficient erosion (M4), the orogen is shallower and narrower after 300 km of shortening (Figure 5d) compared to the moderately eroded M1. The shortening is accommodated by incipient subduction involving the strong lower crust and mantle lithosphere, raising an approximately 1 km high mountain belt. Erosion locally removes the upper crust completely, leading to the uplifting of the lower crust within the mountain range. There are two competing mantle shear zones, both of which are reactivated during the later extensional stage. The formation of an asymmetric rift coincides with the reactivation of the shear zone at the right, characterized by thicker crustal roots and hotter inherited lithosphere (right side of Figure 5d).

When low erodibility is used in model M5, a broad region of thick-skinned thrust sheets spanning 500 km is formed by the end of the shortening phase (Figure 5e). These thrust sheets control the mountain's height, which reaches around 5 km. During extension, rifting localizes in the areas with the thickest crustal roots, with continental breakup eventually happening in the region where the left-most of the three roots is located. The final rifted margin geometries are highly asymmetric: the left margin has a width of approximately 220 km, while the right margin is about 500 km wide (including sections that have been advected beyond the model domain).

Figure 5. Alternative models illustrating how orogenic topography controls the final location of breakup. Note that the times displayed here are model time instead of “Myr ago.” This change allows for easy comparison of model results without reference to geologic evolution. Each panel shows model results at the end of the orogenic phase after a shortening distance of 300 km (left) and the final architecture of the rifted margins after a total extension of 350 km (right). (a) Reference model M1. (b), (c) M2 and M3 with different collision velocities. (d), (e) M4 and M5 with varied surface process efficiency. (f), (g) M6 and M7 with alternative crustal thicknesses. (h) M8, the purely extensional model without orogenic inheritance. Key model parameters are given in Table 1. Above each panel on the left, the width of the mountain belt is indicated by a black line, the crustal roots with higher topography than the surrounding terrain are marked in green and the site of future continental breakup is indicated by a red line. Mountain topography is represented by a blue line, which we convert to gravitational potential energy (see Supporting Information) indicated through the orange axis in panel (a). The Moho depth at the boundary of the necking zone and the hyperextended domain is marked. The temperature isotherm of 1,330°C is shown by a white line in the right panels. Note that a different topographic scale is used in (d) to display variations in elevation. The blue arrows on the left and right sides indicate the shortening phase. Importantly, the location of continental breakup always matches one of the highest mountain ranges.

4.2.3. The Effect of Lithospheric Rheology: Model M6 and M7

Models M6 and M7 feature variations in initial upper crustal thickness. In model M6, the upper and lower crustal thickness is 23 and 17 km, respectively, that is, the upper crust is 2 km thinner while the less radiogenic lower crust is 2 km thicker than in M1. Due to initial thermal equilibration, this difference leads to a colder and therefore stronger lower crust, which induces a more pronounced coupling of the crust and mantle lithosphere. During shortening, two conjugate thrust faults accommodate strain in the central part of the model. Deformation and strain localization occur in narrow domains generating a ~ 300 km wide orogen. These regions have limited topography, measuring less than 4 km, comparable to model M1. The narrow orogens feature three crustal roots with an approximately 55 km thick crust. Finally, continental breakup occurs at the location of the highest mountain range and leads to symmetric rifted margins.

M7 has a 2 km thicker upper crust and a 2 km thinner lower crust than M1 leading to an overall warmer initial lithosphere. Higher crustal temperatures generate a weak lower crust and the decoupling of the crust and mantle lithosphere. Viscous deformation occurs along the decollement between the upper and lower crust (Figure 5g), while strain localization takes place in the plastic upper crust, leading to pervasive thrust faulting. The final crustal thickness is about 60 km, and the orogenic belt is about 600 km wide after 300 km of convergence - considerably wider than in model M1. Breakup is observed on the right side of the former orogen in a region of formerly thick crust. This pair of alternative models M6 and M7 shows that seemingly small changes in crustal configurations can result in drastic changes of the thermal configuration, viscosity structure and hence the architecture of mountain belts and of subsequently forming rifted margins.

4.2.4. The Impact of the Orogenic Phase: Model M8

Model M8 adopts the same configuration as the reference model M1 (Table 1), but omits the shortening stage. Lithospheric extension initiates on a largely homogeneous lithosphere that contains the same random seeding as model M1 and follows the same extension history as model M1 (Figure 5h and Figure S1 in Supporting Information S1).

Both models M1 and M8 generate symmetrical wide rifted margins. However, they exhibit different characteristics in terms of sedimentary basin distribution, lithospheric thickness, and fault properties (Figure S2 in Supporting Information S1). The omission of an orogenic phase in model M8 results in the absence of pre-rift crustal thickening or inherited weaknesses. The initial lower crust in model M8 is thinner, with a thickness of 15 km (the left panel of Figure 5h), compared to the crustal root of model M1 where the lower crust at the onset of extension varies between 20 and 60 km ($x = 200\text{--}500$ km) (the left plane of Figure 5a). Consequently, the lower crust in model M8 exhibits greater lithospheric strength compared to the crustal root areas of the reference model M1. The initial configuration of M1 is sufficiently weak to facilitate the formation of a several hundred kilometers wide rifted margin. The sedimentary basins in M8 cover a narrower domain, with a total width of approximately 100 km (Figure S2c in Supporting Information S1).

In the necking zone and hyperextended domain ($x = 100\text{--}250$ km), the Moho depth of M8 and M1 align well with seismic profile observations of the SCS (Figures S2b and S2c in Supporting Information S1). In addition, the thermal LAB also shows a good match between M1 and M8 from $x = 150\text{--}300$ km (Figure S2a in Supporting Information S1). However, in the proximal domain, the shallower LAB and Moho depth in model M8, compared to M1 (Figures S2a and S2b in Supporting Information S1), can be attributed to the absence of crustal thickening during the orogenic phase. Based on seismic interpretation and gravity inversion data (Bai et al., 2019) the thickness of the lower crust in the northern SCS is approximately 4–18 km. This compares very well to the lower crust thickness in M1, which ranges from 4 to 20 km (Figure 5a), while M8 is much thinner, with a thickness of 4–10 km (Figure 5h). The different geological histories are further reflected in the distinct characteristics of the boundary faults. In model M8, these normal faults evolve into sedimentary basin boundaries whereas the inherited thrust faults are reactivated into sedimentary basin boundaries of model M1 (Figure 3).

5. Discussion

5.1. Comparison to Observations

To assess the applicability of our models to the SCS, we compare them to available geological data sets on the evolution of the Mesozoic Yanshanian orogen and subsequent Late Mesozoic to Cenozoic rifting. We combine

onshore observations and well results, providing petrological and thermochronological data on the pre-rift basement, with present-day structure of rifted margin based on reflection and refraction seismic profiles (see Figure 5).

5.1.1. Comparison of Reference Model M1 to Observations

It is widely accepted that an Andean-type continental margin existed along the present southeastern margin of South China about 100 Myr ago (e.g., S. Li et al., 2012, Z. X. Li et al., 2012). The Andean mountain belt exceeds elevations of 5 km (Riesner et al., 2017), supported by crustal roots that reach depths of 70 km (Introcaso et al., 1992). Additionally, a fold-and-thrust belt developed on both the western and eastern sides of this mountain range (Armijo et al., 2010; Giambiagi et al., 2003; Ramos et al., 2004). Our model reproduces these prominent features of the Andes—it exhibits a peak topography of approximately 4.5 km, a maximum crustal thickness of 80 km, and a distribution of opposite-dipping thrust faults that resembles the first-order orogen style of the Andes (see Figure 3c).

The orogen of model M1 features a topography of about 4.5 km after a shortening of 300 km (Figure 3b). This mountain height is consistent with two different pieces of evidence from the Late Mesozoic transition from convergence to extension: (a) Analysis of basaltic eruptions and the distribution of adakite revealed an estimated paleo-elevation of around 4.7 km for a coastal mountain range in eastern China (Xia et al., 2012). (b) Landscape modeling depicted a coastal mountain range with a peak height of 5 km in the southern East China Sea Continental Shelf around 100 Myr ago (Liu et al., 2022).

The final LAB depth of model M1 is in agreement with geological data sets from the present-day SCS. The LAB marks a conspicuous alteration in the temperature-dependent physical properties of the upper mantle and frequently coincides with the isotherms of approximately 1,200–1,300°C (Artemieva, 2009). Beneath the SCS oceanic basin, the seismic LAB depth is estimated to range between 60 and 70 km (Huang & Xu, 2011), while along the continental margins the seismic LAB increases to a depth of 100 km (Tang & Zheng, 2013). Independent data suggests LAB depths ranging from 65 km in the East Sub-basin to a maximum of 120 km (Chen et al., 2018) at the continental margin (referred to as Line 1 and Line 2 in Figure 6a, location in Figure 1). Defined by the isotherm of 1,330°C, the LAB in our reference model M1 displays varying depths ranging between 65 and 80 km across oceanic basins. It is apparent that there is a pronounced deepening of the modeled LAB beyond 120 km depth in the proximal regions (the red line in Figure 6a).

The final Moho depth of model M1 also closely matches the previously interpreted crustal structure of the present-day SCS region, describing a wide rift mode over 600 km with a succession of hyper-extended basins separated by basement highs. Gravity inversion modeling constrained by Ocean Bottom Seismometer (OBS) data indicates that the Moho depth varies across the region from 10 to 35 km (Bai et al., 2020; Chen et al., 2013). The refraction seismic profile OBS 1993 (Figure 1), which extended from the northern margin of the SCS to the oceanic crust (Figure 6b), revealed Moho depth variations ranging from 25 km within the necking domain to 12 km within the oceanic basin (Yan et al., 2001). Another comprehensive wide-angle OBS2006-3 profile extends further east across the margin (location in Figure 1). Within this profile, the Moho depth shows a gradual seaward shallowing (Figure 6b), ranging from 25 to 17 km (Wie et al., 2011). In our reference model M1, the Moho depth gradually becomes shallower toward the sea, measuring approximately 10–13 km in the hyperextended domain, 15–25 km in the necking zone, and 32–35 km in the proximal domain. Notably, the Moho depth undergoes sudden changes in regions associated with lower crustal exhumation (Figure 6b).

Model M1 features the occurrence of a succession of rift basins filled by Late Cretaceous to Cenozoic sediments showing wedge-shaped geometries within tilted blocks (Figure 6) that align with seismic profiles collected in the northern margin of the SCS (Yang et al., 2018). In M1, fully reactivated thrust faults evolve into normal faults, serving as the boundaries of sedimentary basins (Figure 6d). Reactivation of pre-existing Mesozoic thrust faults during Cenozoic rifting has been well documented, notably, in the PRMB thanks to reflection seismic and well data (Camanni & Ye, 2021; Deng et al., 2021; Ye et al., 2018). There, the continental basement consists of crystalline rocks with several magmatic intrusions associated with Mesozoic sedimentary successions both being recovered in several wells across the PRMB (Figure 6e). This basement shows distinct reflective packages that have been linked by several authors to pre-rift thrusts formed during the Mesozoic orogeny (Deng et al., 2021; Guan et al., 2023; Ye et al., 2018) (Figure 6e). Some of these thrusts are sealed and crosscut by an unconformity

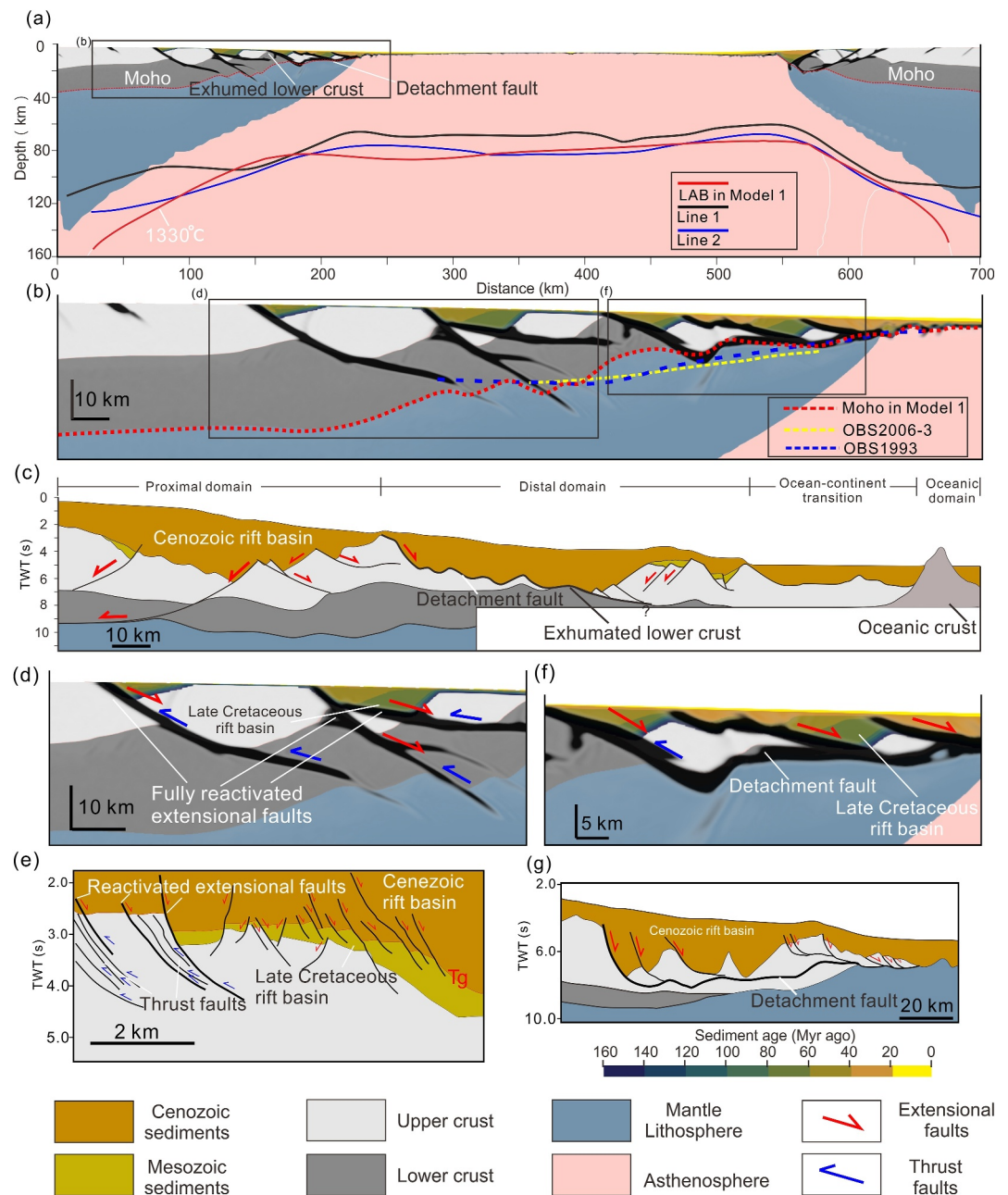


Figure 6. Comparison between data from the South China Sea (SCS) and the reference model M1. (a) Comparison of lithosphere-asthenosphere boundary (LAB) depth. Line 1 and Line 2 designate geophysical profiles used to obtain lithospheric structures across the SCS (see Figure 1 for their location, Chen et al., 2018). For the comparison with seismic data, the LAB depth is here defined by the thermal properties, specifically by a temperature isotherm of 1,330°C in Line 1 and Line 2. (b) Moho depth comparison. OBS 1993 (Yan et al., 2001) and OBS 2006-3 (Wie et al., 2011) represent the northern margin structure of the SCS (see Figure 1 for position). (c) Lower crust exhumation in the distal domain of Line 5 (Deng et al., 2020). (d), (f) Fully reactivated extensional faults and sediment basins of M1 highlighted in close-up views. Detachment faults have been rotated to low angles in panels (f). (e) Interpreted seismic sections of Line 3 and 4 in Figure 1 depicting reactivated thrust faults (Ye et al., 2018). Tg represents the regional unconformity between pre-Cenozoic and Cenozoic structural units (Ye et al., 2018). (g) The detachment fault flattens at approximately 7 s two-way travel time (TWT) with a sudden thinning of the continental crust (Line 4 in Figure 1, Yang et al., 2018). Sediments in panels (b, d, and f) are colored according to their age as shown in the color bar.

Table 2
Comparison of Key Geological Features of the South China Sea and Model Results

Key geological features	M1	M2	M3	M4	M5	M6	M7	M8
Orogenic height after shortening	✓	✗	✓	✗	✗	✓	✓	✗
Reactivation of thrust faults	✓	✓	✓	✓	✓	✓	✓	✗
Mesozoic sedimentary basins	✓	✓	✓	✓	✓	✓	✓	✗
Wide sedimentary basin distribution	✓	✓	✓	✗	✓	✗	✓	✗
Low angle detachment faults	✓	✓	✗	✓	✗	✓	✗	✓
Exhumed lower crust	✓	✓	✗	✓	✗	✓	✗	✓
Region of hyper-extended domain	✓	✓	✓	✓	✗	✓	✗	✓
Symmetric rifted margin	✓	✗	✗	✓	✗	✓	✗	✓
Comparable Moho depth	✓	✗	✗	✓	✗	✓	✓	✓
Comparable LAB depth	✓	✗	✗	✓	✗	✓	✗	✓

Note. The checkmark (✓) indicates comparable features, while the cross (✗) denotes features that are not reproduced. See Figure 5 and Figure S3 in Supporting Information S1 for more details. We chose M1 as our reference model, because it is the only one that fulfills all of these constraints.

(marked Tg on Figure 6e) and overlain by Cenozoic sediments. However, in other locations, the thrusts are reactivated as Cenozoic normal faults delimiting new Cenozoic rift basins.

The distal domain of M1 is characterized by a succession of detachment faults (i.e., low-angle normal faults) resulting from footwall rotation that interacted with lower crustal thrust faults (Figure 6f), which is very similar to observations of the interpreted seismic profile shown in Figure 6g. Indeed, the SCS distal margin records the formation of hyper-extended basins controlled by low-angle detachment fault accommodating large displacement such as the Liwan and Baiyun sag basins (Lei et al., 2019; Zhang et al., 2020; Zhao et al., 2018).

The exhumation of lower crustal materials in the footwall of detachment faults, as observed in the northern margin of the SCS (Deng et al., 2020), is also reproduced by our reference model. Rift-related exhumation of lower crustal rocks is enhanced in domains formerly located in the central mountain region (Movie S1a). These detachment faults accommodate the exhumation of lower crust close to or at the surface. Such exhumation has been inferred notably on the Liwan sag based on high-resolution seismic data along metamorphic core-complex-like structures (Figure 6c) and is coherent with our model M1 (Figure 6b). More generally, our modeling results emphasize the importance of former thrust faults or inherited structures for the development of low-angle normal faulting as reported by previous studies (Figure 6e, Deng et al., 2021).

5.1.2. Comparison of Alternative Models to Observations

We consider a model for the SCS successful when it accurately reproduces the following key geological features: (a) the orogenic height during the convergent stage, (b) the reactivation of thrust faults, (c) a comparable age and (d) structure of sedimentary basins, (e) the presence of detachment faults, (f) exhumed lower crust, (g) a region of hyper-extended crust, (h) rifted margin symmetry, (i) the depth of the Moho, and (j) the present-day LAB-depth. Table 2 evaluates each of the seven alternative models based on these criteria.

The Andean-type orogen in our study region reached an elevation of approximately 5 km during the late Mesozoic, prior to the formation of the SCS (Liu et al., 2022; Xia et al., 2012). Apart from model M1, only models M3, M6, and M7 generate orogenic topography consistent with this elevation, with models M2 and M4 predicting significantly lower topography, and model M5 displaying somewhat higher peak elevations. Model M2, characterized by a low shortening velocity, allows for a longer period of erosion, leading to a low mountain terrain (Figure 5c), whereas the high erosion rates of Model M4 locally remove the upper crust, producing an approximately 1 km high mountain belt (Figure 5d). In contrast, in the low erosion scenario of model M5, the topography exceeds 5 km, reaching a maximum of 5.5 km at specific locations ($x = 340$ km and $x = 450$ km) (Figure 5e). These results highlight the significant influence of shortening velocity and erosion efficiency on shaping the orogenic topography.

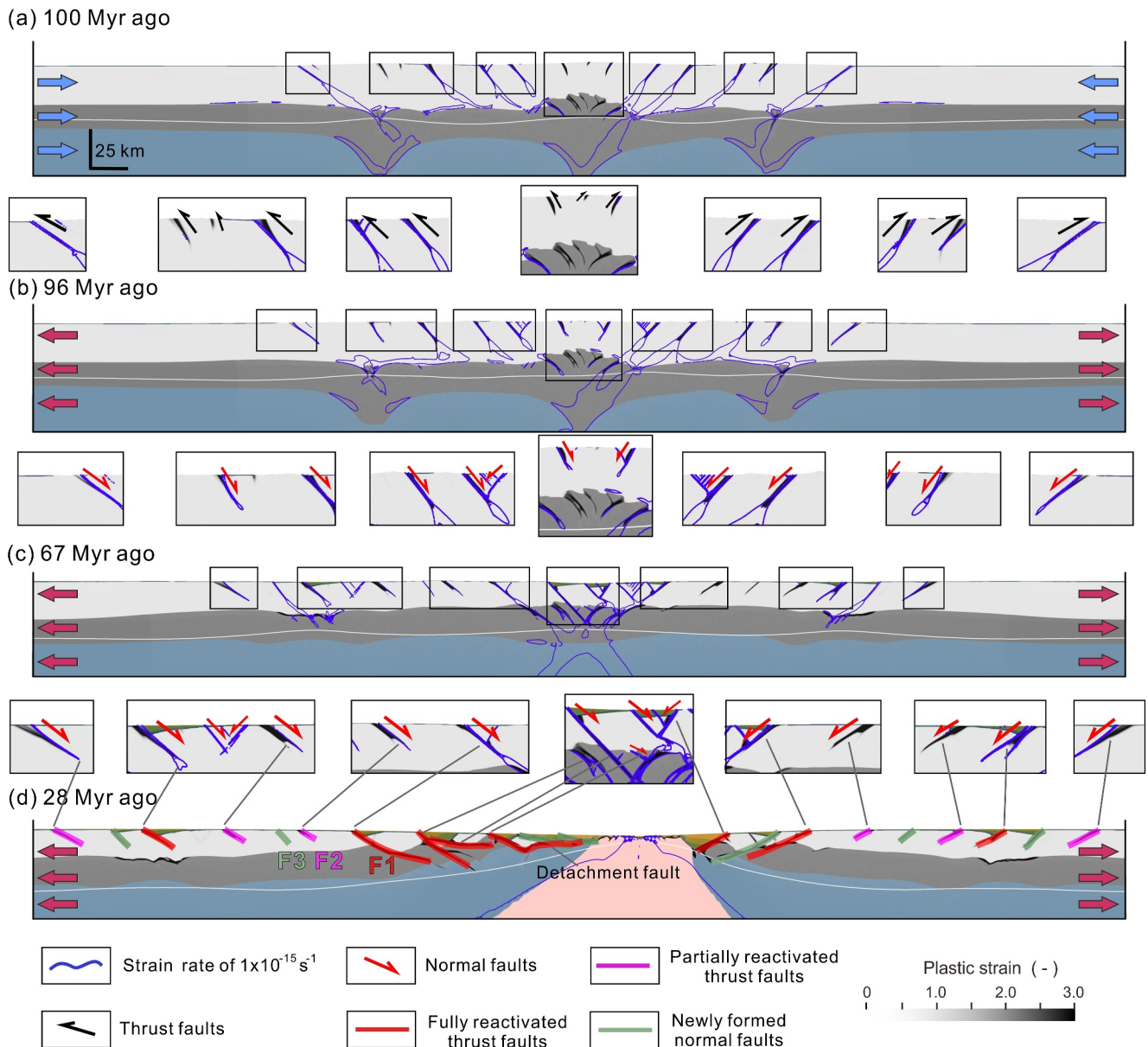


Figure 7. Thrust fault reactivation analysis of reference model M1. (a) The lithospheric structures after 300 km of convergence. The black boxes are specific areas selected for closer examination of thrust faults. The blue line represents the current fault activity, contouring a strain rate of $1 \times 10^{-15} \text{ s}^{-1}$. Black half arrows indicate hanging wall movement of thrust faults. (b) and (c) The reactivation of thrust faults during extension. The white line shows the temperature isotherm of 600°C . Red half arrows show the motion of the hanging wall of normal faults. (d) Three fault types are identified: newly formed normal faults (in green, such as F3), partially reactivated thrust faults (in pink, such as F2), and fully reactivated thrust faults (in red, such as F1). The fully reactivated thrust faults form the boundaries of sedimentary basins. The blue arrows on the left and right sides indicate the shortening phase and the red arrows show the extension phase. Note that the underlying figures in a, b and c are zoom-in views of the cross-section, following the same order as the black boxes in the cross-sections. For more information, refer to Movie S1.

The final rifted margin architectures of the alternate models (Figure 5) differ significantly from the SCS. Figure S3 in Supporting Information S1 compares Moho and thermal LAB depth between the alternative model results and geophysical data. For the sake of brevity, we only compare the three models that generate orogenic topography of around 5 km, resembling the late Mesozoic orogen with observations from the present-day SCS. The high shortening velocity model (M3) produces an asymmetric rifted margin with a deeper Moho (>30 km) in the necking zone compared to geophysical data. Additionally, it lacks both detachment faults and exhumed lower crust (Figure 5c). In contrast, the thin upper crust model (M6) generates a symmetric rift with Moho depths of 12–17 km in the hyperextended domain (Figure 5f), comparable to the observations from the SCS. However, the

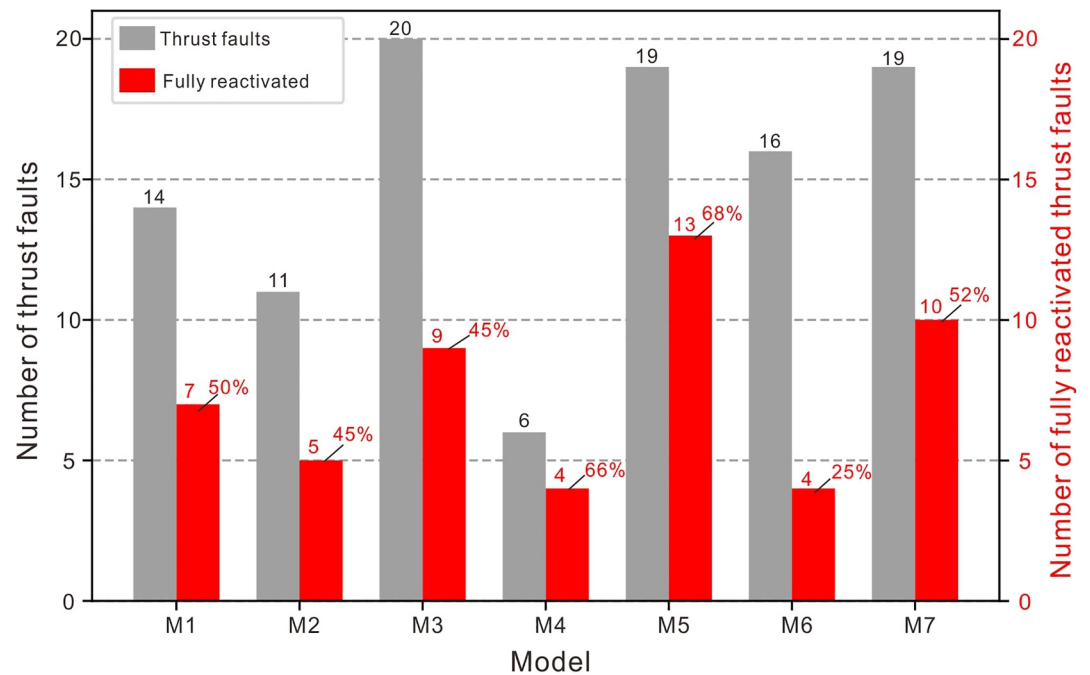


Figure 8. The number and percentage of reactivated thrust faults for various model parameters. The gray column displays the number of inherited thrust faults after a shortening distance of 300 km. The red column displays the number of fully reactivated thrust faults. The percentage of fully reactivated out of all thrust faults is indicated in red. See Figure 7 and Table 1 for the differences between models M1 to M7. Note that model M5, with low erosion efficiency, has the greatest percentage of fully reactivated thrust faults. There are a total of 17 normal faults in M8 (Figure 5h), but no reactivated thrust faults. Therefore, M8 is not represented in this figure.

Moho depth in the necking domain of this model is deeper than in the natural study area. M6 does display exhumed lower crust and rotated lower-angle detachment faults (Figures 5c and 5g), mirroring observations in the SCS. Finally, the thick upper crust model M7 resembles M3 with a comparatively deep Moho and it lacks critical features, such as detachment faults and exhumed lower crust (Figure 5g). These results highlight the importance of the initial crustal configuration in shaping the final rifted margin structures.

Our comprehensive comparison reveals that model M6 (thin upper crust) yields results similar to the reference model M1. Despite the initial difference in upper crust thickness, both models experience significant crustal thickening and thermal weakening during shortening. This suggests that the orogenic phase may erase the initial thickness disparity, leading to comparable rifted margin architectures for the SCS in both models.

5.2. Fault-Scale Inheritance

It has long been known that former thrust faults can be reactivated as normal faults during extension (Allmendinger et al., 1983; Brun & Choukroune, 1983). According to previous studies, the reactivation of such a pre-existing fault mainly depends on the fault's strength, which correlates with accumulated strain (Deng et al., 2021; Henza et al., 2010; Wang et al., 2021), the amount of tectonic compression (Salazar-Mora et al., 2018), but also the extension direction (Bonini et al., 1997; Keep & McClay, 1997; Molnar et al., 2019). For the northern rifted margin of the SCS, the angle between the extension direction and the strike of pre-existing faults plays a role in their reactivation, with higher angles increasing the likelihood of reactivation (Ye et al., 2020). Throughout the convergence phase of the Wilson cycle, thrust faults evolve and accumulate strain, contributing to the weakening of the lithosphere (e.g., Handy & Brun, 2004; Oncken et al., 2012). In this section, we quantify the reactivation of thrust faults in our models and identify the factors that control the process during the transition from convergence to extension.

Reactivation of pre-rift thrust faults has been categorized into two modes: partial and full reactivation (Deng et al., 2021; Guan et al., 2023). In the case of fully reactivated thrust faults, the faults increase in length and displacement and eventually evolve into basin-bounding faults (e.g., F1 in Figure 7d). Conversely, partially

reactivated thrust faults experience limited displacement during the rifting stage, resulting in insufficient space for sediment accumulation (e.g., F2 in Figure 7d).

We present a statistical analysis focusing on fully reactivated pre-rift thrust faults, which we compare to the total number of inherited thrust faults after 300 km of shortening across the seven presented models (Figure 8). We find that not all of the inherited thrust faults experience full reactivation. From Figure 8, we can see that between 25% and 68% of the thrust faults are fully reactivated, with an average of approximately 50%. The highest percentage of full reactivation is observed in model M5, characterized by a low erosion efficiency ($K_f = 1 \times 10^{-6} \text{ m}^{0.2}/\text{yr}$, Table 1), while the lowest percentage is found in model M6, the colder model with a thin initial upper crust (Table 1).

We find a characteristic distribution of fully reactivated faults, such that the reactivation potential of pre-rift thrust faults is significantly higher at high-elevation core regions of the orogens compared to those at mountain flanks (Figure 7d). This trend translates to an increase in accumulated strain from proximal to distal domain (Cowie et al., 2005; Ebinger, 2005). We find that reactivation is strongly influenced by the thermal inheritance, where regions with overthickened crustal roots experience thermal weakening, locally reducing the lithospheric strength. In such areas, inherited thrust faults have a higher tendency for full reactivation, such as fault F1 (Figure 7d). In summary, strain accumulation plays a role in the early stages of reactivation and applies to fully and partially reactivated thrust faults. Inherited thermal weakness on the other hand is the dominant factor controlling the full reactivation of thrust faults as only faults located in the weakest segments of the lithosphere are fully reactivated.

5.3. Orogen-Scale Inheritance

During tectonic convergence, the shortening of the lithosphere causes the orogenic crust to thicken and to develop pronounced topography, leading to a significant increase in GPE gradients (Jones et al., 1996; Molnar & Lyon-Caen, 1988) and a weakening of the lithosphere (Dewey, 1988). This build-up of high GPE is a major contributor to lithospheric buoyancy forces (Coblentz et al., 1994). The numerical modeling results for southwestern North America indicate that the presence of high GPE associated with a thickened crustal root is the primary factor causing orogenic collapse and subsequent rifting (Bahadori et al., 2022).

After 300 km of convergence, all presented models exhibit diverse mountain geometries in terms of width, height, and distribution of thrust faults (Figure 5). To evaluate the process of continental breakup, we calculate the GPE per unit area for the model M1 (see Supporting Information S1, England et al., 2016; Haxby & Turcotte, 1978; Jones et al., 1996). Along the model M1 profile, the mountain range holds a significantly elevated GPE, estimated to be 3 to 5 TN m^{-1} (Figure 5a). GPE is particularly high within the central crustal root regions where continental breakup will occur. Our models hence indicate that the high GPE gradients give rise to deviatoric stress within the gravitationally unstable crustal root areas (Schott & Schmeling, 1998; Zoback & Mooney, 2003), contributing to orogen collapse and further continental breakup (Bialas et al., 2007; Hetzel et al., 1995).

During tectonic convergence, the thickening of the orogenic crust in conjunction with radiogenic heat production leads to increased temperatures in the crust (England & Thompson, 1984). Given the highly non-linear relationship between temperature and rock viscosity (Gerya, 2010), an increase in temperature causes a significant, simultaneous, decrease in lithospheric viscosity and integrated strength. In model M1, a clear trend of crustal thickening is observed during the shortening phase, with crustal thickness ranging from 60 to 80 km within three specific crustal root domains. These domains slowly warm up due to radioactive decay within the crust (Pysklywec & Beaumont, 2004). The lower thermal conductivity of crustal rocks compared to mantle rocks prevents efficient heat transfer within a thickening crust, which leads to further heat accumulation and increased crustal temperatures during thickening (Bahadori et al., 2022). Consequently, the overall strength of the crust is reduced in these specific regions.

In our models, the localization of rift systems within orogens is primarily driven by variations in crustal thickness. Thick crust consistently coincides with high GPE, high crustal temperatures and hence low strength. The relative impact of lateral variations in driving force and strength in this convoluted system of dynamic feed-back loops is difficult to deduce. Nevertheless, our study clearly shows that continental breakup in all models occurs within thick crustal root areas. In all models, multiple areas of thick crust exist, which leads to a dynamic competition

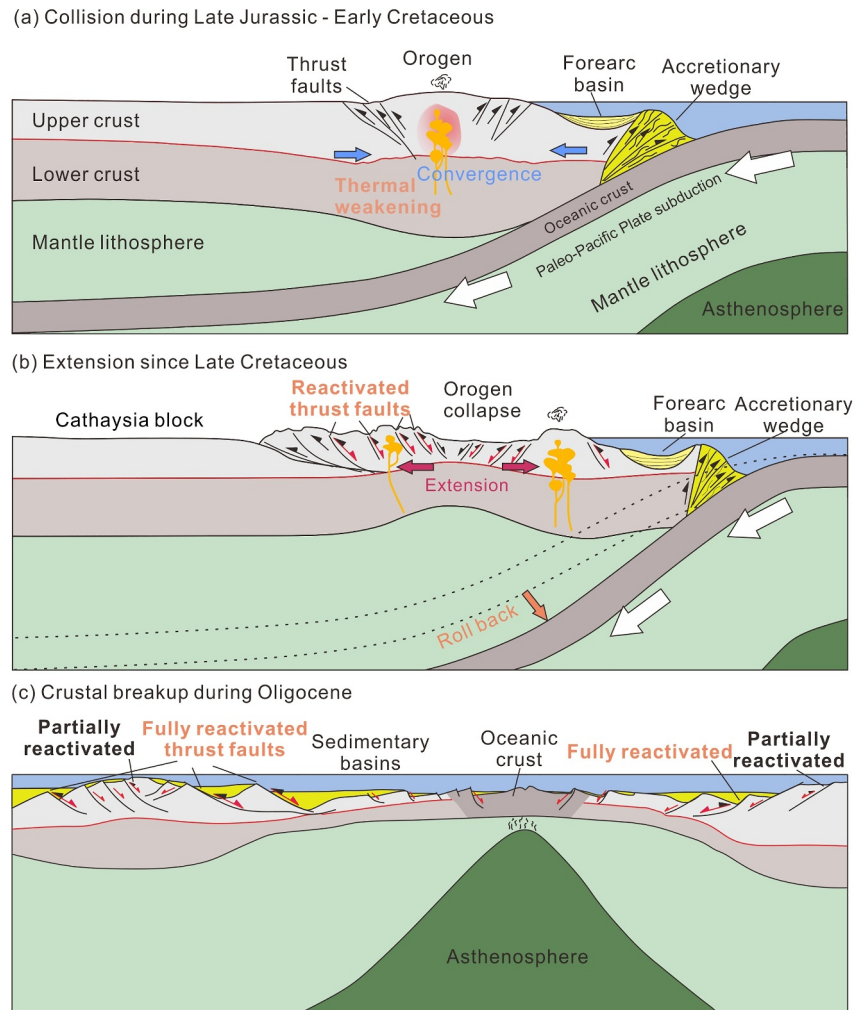


Figure 9. Conceptual sketch of evolution from orogen to rifted margin in the South China Sea (SCS) region. (a) Crustal thickening, mountain building and thrust faulting associated with the subduction of Paleo-Pacific Plate since Late Jurassic. (b) Collapse of orogen and development of extensional basins as a result of slab rollback since Late Cretaceous. Some pre-existing thrust faults are reactivated. (c) Continental breakup and seafloor spreading occurred during latest early Oligocene. Fully reactivated thrust faults serve as basin boundaries in the SCS. Images modified from Larsen et al. (2018) and Suo et al. (2019).

between lateral weaknesses. Inherited thrust faults within regions of future breakup always experience the highest amount of post-orogenic extensional strain and are therefore consistently slated for full reactivation.

5.4. Impact of Inherited Structures on the Evolution of the South China Sea

Integrating observations and modeling results, we here present a conceptual model that illustrates how the presence of inherited structures influences the geometry and evolution of the SCS (Figure 9). Mesozoic shortening along the South China margin resulted in an Andean-type margin with extensive crustal thickening associated with a series of thrust faults (Figure 9a). Similar to the SCS, our models dynamically produce a rift in heterogeneous lithosphere that contains a 4.5 km high orogen, an overthickened crust (~80 km), and a series of pre-existing thrust faults that accommodate high strain localization (Figure 3b). While the southern region of the South China underwent mountain building and thickening, the crust maintained an abnormally high temperature and possessed a substantial GPE prompted by lateral variations in topography, density and thickness. These circumstances predict the primary lithospheric inheritance of the SCS in the Late Mesozoic.

The South China continental margin underwent a transition from an Andean-type continental margin to a Western Pacific-type margin due to slab roll-back and an increased subduction dip angle since the Late Cretaceous (He & Xu, 2012; S. Li et al., 2012; Z. X. Li et al., 2012; Wang & Shu, 2012; Zhou & Li, 2000). Oceanward trench retreat resulted in the collapse of coastal mountains, extensional reactivation of thrust faults, and lower crustal exhumation through detachment faulting (Figures 3e and 9b). The observed reactivation of inherited fault systems in the SCS controls the geometry of fault systems and their associated half-grabens (Camanni & Ye, 2022). The seismic observations reveal that extensional faults exhibit a WNW- to EW- and ENE-trend, influenced by the thrust system in the north of the SCS (Ye et al., 2020). Our model M1 shows that fully reactivated thrust faults enable the formation of deep fault-bounded basins (Figure 7d). Reactivated pre-existing structural features act as nucleation sites for the initiation of new normal faults such as fault F3 in our models (Figure 7d).

With the opening of the SCS during the Early Oligocene (around 32 Myr ago), previously orogenic regions experienced continental breakup facilitated by extensional forces induced by high GPE, thermal weakening, and the localization of reactivated thrust faults (Figure 9c). In the distal margins, normal faults underwent major rotation, ultimately resulting in the development of low-angle detachment faults (e.g., Figure 7d). This process explains the reactivation of Mesozoic thrust faults and how they evolve to detachment faults in the SE of the PRMB, which root in the interface between the upper and lower crust (Savva et al., 2014). There is an increased likelihood of reactivating pre-existing thrusts in close proximity to the rift center of the SCS (Deng et al., 2021; Wang et al., 2018). Indeed, model M1 has the highest concentration of fully reactivated thrust faults around the rift center (Figure 7d). These regions are primarily orogenic, where the behavior of inherited thrust faults is influenced by the thermal weakening via various heating mechanisms. Our models further corroborate that the wide rifted margin of the SCS is formed due to reduced lithosphere strength (Brune, Heine, et al., 2017; Clift et al., 2002) induced by inherited weaknesses. The tectonic evolution of the SCS is significantly impacted by multi-scale inheritance, which controls the reactivation of thrust faults, continental breakup, and rifted margin architectures.

Similar to the SCS, the Trøndelag Platform of the Mid-Norwegian rifted margin shows a complex evolution recording the transition from orogenic collapse to rifting (Peron-Pinvidic et al., 2020). This region exhibits core-complex geometries associated with intense shearing in relation with detachment faults (Peron-Pinvidic et al., 2020). The Aegean Sea and Western Anatolia exhibit prime examples of continental metamorphic core complexes, where lower crust has been exhumed along normal faults (Bodur et al., 2023; Jolivet et al., 2013). Extension in this region is driven by the retreat of Hellenic subduction zones (Le Pichon & Angelier, 1981) and the GPE stored in the thick Hellenic crust (Malinverno & Ryan, 1986). Just like in the SCS, inherited orogenic structures played a major role in shaping these extensional regions. These observations illustrate the broader applicability of our modeling findings globally, emphasizing the impact of orogenic inheritance on rift evolution.

6. Conclusions

We employed numerical modeling to investigate how orogenic inheritance impacts the evolution of rifts and rifted margins. Our three main conclusions are: (a) By integrating successive shortening and extensional phases into our numerical models, we successfully generate rifted margin architectures that are consistent with geophysical observations in the SCS. These models reproduce and explain first-order characteristics of the SCS rifted margins, such as crustal and lithospheric thicknesses, a hyperextended domain characterized by the exhumation of lower crust through detachment faulting, and basin boundaries marked by fully reactivated thrust faults (Figure 6). (b) Reactivation of thrust faults is affected by several factors, such as the amount of inherited strain, strain competition between simultaneously active faults and thermal weakening. Full reactivation of thrust faults and the formation of basin-bounding inverted faults is however governed by thermal inheritance (Figure 7). (c) Lithospheric inheritance exerts a notable influence on both the initiation of rifting and the final architecture of rifted margins. We find that rift localization in orogens is primarily controlled by variations in crustal thickness. Thick crust is associated with high GPE, increased temperatures, and reduced strength. In all our models considering orogenic inheritance (M1-M7), continental breakup consistently occurs in regions characterized by thick crustal roots (Figure 5). Our findings suggest that orogenic inheritance plays a major role in shaping rifted margins, which should apply to other rifts formed in mountain belts, like the Norwegian rifted margin, the Aegean Sea and Western Anatolia.

Data Availability Statement

The software and input files are available at Li (2024a). The data for GPE calculation and P-T-t path of Model M1 can be found at Li (2024b). Figures were made using ParaView 5.11.0, Generic Mapping Tools (Wessel et al., 2019), Coreldraw X7, and Python 3.7.

Acknowledgments

We thank the Computational Infrastructure for Geodynamics (geodynamics.org), which is funded by the National Science Foundation under award EAR-0949446 and EAR-1550901, for supporting the development of ASPECT. KL acknowledges financial support from the China Scholarship Council (CSC). SB has been funded by the European Union (ERC, EMERGE, 101087245). AG was funded by the Helmholtz Association (Recruitment Initiative 0316). We gratefully acknowledge the computing time granted by the Resource Allocation Board and provided on the supercomputer Lise at NHR@ZIB as part of the NHR infrastructure. The calculations for this research were conducted with computing resources under the project bbp00039. KL thanks Frederik Tilmann for discussions of deep lithosphere structure of the research region. We thank an anonymous reviewer, Magali Billen, the associated editor, and editor Anke Friedrich for their constructive comments that contributed to improving the manuscript. Open Access funding enabled and organized by Projekt DEAL.

References

- Allmendinger, R. W., Sharp, J. W., Von Tish, D., Serpa, L., Brown, L., Kaufman, S., et al. (1983). Cenozoic and Mesozoic structure of the eastern Basin and Range province, Utah, from COCORP seismic-reflection data. *Geology*, *11*(9), 532. [https://doi.org/10.1130/0091-7613\(1983\)11<532:CAMSOT>2.0.CO;2](https://doi.org/10.1130/0091-7613(1983)11<532:CAMSOT>2.0.CO;2)
- Argus, D. F., Gordon, R. G., & DeMets, C. (2011). Geologically current motion of 56 plates relative to the no-net-rotation reference frame. *Geochemistry, Geophysics, Geosystems*, *12*(11), Q11001. <https://doi.org/10.1029/2011GC003751>
- Armijo, R., Rauld, R., Thiele, R., Vargas, G., Campos, J., Lacassin, R., & Kausel, E. (2010). The West Andean thrust, the San Ramon fault, and the seismic hazard for Santiago, Chile. *Tectonics*, *29*(2), TC2007. <https://doi.org/10.1029/2008TC002427>
- Artemieva, I. M. (2009). The continental lithosphere: Reconciling thermal, seismic, and petrologic data. *Lithos*, *109*(1–2), 23–46. <https://doi.org/10.1016/j.lithos.2008.09.015>
- Audet, P., & Bürgmann, R. (2011). Dominant role of tectonic inheritance in supercontinent cycles. *Nature Geoscience*, *4*(3), 184–187. <https://doi.org/10.1038/ngeo1080>
- Bahadori, A., Holt, W. E., Austermann, J., Campbell, L., Rasbury, E. T., Davis, D. M., et al. (2022). The role of gravitational body forces in the development of metamorphic core complexes. *Nature Communications*, *13*(1), 5646. <https://doi.org/10.1038/s41467-022-33361-2>
- Bai, Y., Dong, D., Brune, S., Wu, S., & Wang, Z. (2019). Crustal stretching style variations in the northern margin of the South China Sea. *Tectonophysics*, *751*, 1–12. <https://doi.org/10.1016/j.tecto.2018.12.012>
- Bai, Y., Wang, X., Dong, D., Brune, S., Wu, S., & Wang, Z. (2020). Symmetry of the South China Sea conjugate margins in a rifting, drifting and collision context. *Marine and Petroleum Geology*, *117*, 104397. <https://doi.org/10.1016/j.marpetgeo.2020.104397>
- Barckhausen, U., Engels, M., Franke, D., Ladage, S., & Pubellier, M. (2014). Evolution of the South China Sea: Revised ages for breakup and seafloor spreading. *Marine and Petroleum Geology*, *58*, 599–611. <https://doi.org/10.1016/j.marpetgeo.2014.02.022>
- Beaumont, C., Jamieson, R. A., Nguyen, M. H., & Medvedev, S. (2004). Crustal channel flows: 1. Numerical models with applications to the tectonics of the Himalayan-Tibetan orogen. *Journal of Geophysical Research*, *109*(B6), 2003JB002809. <https://doi.org/10.1029/2003JB002809>
- Bialas, R. W., Buck, W. R., Studinger, M., & Fitzgerald, P. G. (2007). Plateau collapse model for the transantarctic mountains–West Antarctic rift system: Insights from numerical experiments. *Geology*, *35*(8), 687–690. <https://doi.org/10.1130/G23825A.1>
- Bird, P. (2003). An updated digital model of plate boundaries. *Geochemistry, Geophysics, Geosystems*, *4*(3), 1027. <https://doi.org/10.1029/2001GC000252>
- Bodur, Ö., Göğüş, O. H., Brune, S., Uluocak, E. Ş., Glerum, A., Fichtner, A., & Sözbilir, H. (2023). Crustal flow driving twin domes exhumation and low-angle normal faulting in the Menderes Massif of western Anatolia. *Earth and Planetary Science Letters*, *619*, 118309. <https://doi.org/10.1016/j.epsl.2023.118309>
- Bonini, M., Souriot, T., Boccaletti, M., & Brun, J. P. (1997). Successive orthogonal and oblique extension episodes in a rift zone: Laboratory experiments with application to the Ethiopian Rift. *Tectonics*, *16*(2), 347–362. <https://doi.org/10.1029/96TC03935>
- Braun, J., & Willett, S. D. (2013). A very efficient O(n), implicit and parallel method to solve the stream power equation governing fluvial incision and landscape evolution. *Geomorphology*, *180*, 170–179. <https://doi.org/10.1016/j.geomorph.2012.10.008>
- Briais, A., Patriat, P., & Tapponnier, P. (1993). Updated interpretation of magnetic anomalies and seafloor spreading stages in the South China Sea: Implications for the Tertiary tectonics of Southeast Asia. *Journal of Geophysical Research*, *98*(B4), 6299–6328. <https://doi.org/10.1029/92JB02280>
- Brun, J., & Choukroune, P. (1983). Normal faulting, block tilting, and décollement in a stretched crust. *Tectonics*, *2*(4), 345–356. <https://doi.org/10.1029/TC002i004p00345>
- Brune, S., Corti, G., & Ranalli, G. (2017). Controls of inherited lithospheric heterogeneity on rift linkage: Numerical and analog models of interaction between the Kenyan and Ethiopian rifts across the Turkana depression. *Tectonics*, *36*(9), 1767–1786. <https://doi.org/10.1002/2017TC004739>
- Brune, S., Heine, C., Clift, P. D., & Pérez-Gussinyé, M. (2017). Rifted margin architecture and crustal rheology: Reviewing iberia-newfoundland, central South Atlantic, and South China Sea. *Marine and Petroleum Geology*, *79*, 257–281. <https://doi.org/10.1016/j.marpetgeo.2016.10.018>
- Brune, S., Kolawole, F., Olive, J.-A., Stamps, D. S., Buck, W. R., Buitter, S. J. H., et al. (2023). Geodynamics of continental rift initiation and evolution. *Nature Reviews Earth & Environment*, *4*(4), 235–253. <https://doi.org/10.1038/s43017-023-00391-3>
- Brune, S., Williams, S. E., Butterworth, N. P., & Müller, R. D. (2016). Abrupt plate accelerations shape rifted continental margins. *Nature*, *536*(7615), 201–204. <https://doi.org/10.1038/nature18319>
- Buitter, S. J., & Torsvik, T. H. (2014). A review of Wilson cycle plate margins: A role for mantle plumes in continental break-up along sutures? *Gondwana Research*, *26*(2), 627–653. <https://doi.org/10.1016/j.gr.2014.02.007>
- Camanni, G., & Ye, Q. (2022). The significance of fault reactivation on the Wilson cycle undergone by the northern South China Sea area in the last 60 Myr. *Earth-Science Reviews*, *225*, 103893. <https://doi.org/10.1016/j.earscirev.2021.103893>
- Chen, L., Zhang, Z., & Song, H. (2013). Weak depth and along-strike variations in stretching from a multi-episodic finite stretching model: Evidence for uniform pure-shear extension in the opening of the South China Sea. *Journal of Asian Earth Sciences*, *78*, 358–370. <https://doi.org/10.1016/j.jseaes.2012.12.033>
- Chen, M., Fang, J., & Cui, R. (2018). Lithospheric structure of the South China Sea and adjacent regions: Results from potential field modelling. *Tectonophysics*, *726*, 62–72. <https://doi.org/10.1016/j.tecto.2018.01.021>
- Clerc, C., Ringenbach, J.-C., Jolivet, L., & Ballard, J.-F. (2018). Rifted margins: Ductile deformation, boudinage, continentward-dipping normal faults and the role of the weak lower crust. *Gondwana Research*, *53*, 20–40. <https://doi.org/10.1016/j.gr.2017.04.030>
- Clift, P., Lin, J., & Barckhausen, U. (2002). Evidence of low flexural rigidity and low viscosity lower continental crust during continental break-up in the South China Sea. *Marine and Petroleum Geology*, *19*(8), 951–970. [https://doi.org/10.1016/S0264-8172\(02\)00108-3](https://doi.org/10.1016/S0264-8172(02)00108-3)
- Coblentz, D. D., Richardson, R. M., & Sandiford, M. (1994). On the gravitational potential of the Earth's lithosphere. *Tectonics*, *13*(4), 929–945. <https://doi.org/10.1029/94TC01033>

- Corti, G., van Wijk, J., Cloetingh, S., & Morley, C. K. (2007). Tectonic inheritance and continental rift architecture: Numerical and analogue models of the East African Rift system. *Tectonics*, 26(6), TC6006. <https://doi.org/10.1029/2006TC002086>
- Cowie, P. A., Underhill, J. R., Behn, M. D., Lin, J., & Gill, C. E. (2005). Spatio-temporal evolution of strain accumulation derived from multi-scale observations of late Jurassic rifting in the northern North Sea: A critical test of models for lithospheric extension. *Earth and Planetary Science Letters*, 234(3–4), 401–419. <https://doi.org/10.1016/j.epsl.2005.01.039>
- DeMets, C., Gordon, R. G., & Argus, D. F. (2010). Geologically current plate motions. *Geophysical Journal International*, 181(1), 1–80. <https://doi.org/10.1111/j.1365-246X.2009.04491.x>
- Deng, C., Zhu, R., Han, J., Shu, Y., Wu, Y., Hou, K., & Long, W. (2021). Impact of basement thrust faults on low-angle normal faults and rift basin evolution: A case study in the Enping sag, Pearl River Basin. *Solid Earth*, 12(10), 2327–2350. <https://doi.org/10.5194/se-12-2327-2021>
- Deng, H., Ren, J., Pang, X., Rey, P. F., McClay, K. R., Watkinson, I. M., et al. (2020). South China Sea documents the transition from wide continental rift to continental break up. *Nature Communications*, 11(1), 4583. <https://doi.org/10.1038/s41467-020-18448-y>
- Dewey, J. F. (1988). Extensional collapse of orogens. *Tectonics*, 7(6), 1123–1139. <https://doi.org/10.1029/TC007i006p01123>
- Döhmann, M. J. E. A., Brune, S., Nardini, L., Rybacki, E., & Dresen, G. (2019). Strain localization and weakening processes in viscously deforming rocks: Numerical modeling based on laboratory torsion experiments. *Journal of Geophysical Research: Solid Earth*, 124(1), 1120–1137. <https://doi.org/10.1029/2018JB016917>
- Dunbar, J. A., & Sawyer, D. S. (1988). Continental rifting at pre-existing lithospheric weaknesses. *Nature*, 333(6172), 450–452. <https://doi.org/10.1038/333450a0>
- Duret, T., Petri, B., Mohn, G., Schmalholz, S. M., Schenker, F. L., & Müntener, O. (2016). The importance of structural softening for the evolution and architecture of passive margins. *Scientific Reports*, 6(1), 38704. <https://doi.org/10.1038/srep38704>
- Ebinger, C. (2005). Continental break-up: The East African perspective. *Astronomy and Geophysics*, 46(2), 2.16–2.21. <https://doi.org/10.1111/j.1468-4004.2005.46216.x>
- England, P., Houseman, G., & Nocquet, J.-M. (2016). Constraints from GPS measurements on the dynamics of deformation in Anatolia and the Aegean. *Journal of Geophysical Research: Solid Earth*, 121(12), 8888–8916. <https://doi.org/10.1002/2016jb013382>
- England, P. C., & Thompson, A. B. (1984). Pressure—Temperature—Time paths of regional metamorphism I. Heat transfer during the evolution of regions of thickened continental crust. *Journal of Petrology*, 25(4), 894–928. <https://doi.org/10.1093/petrology/25.4.894>
- Fan, C., Xia, S., Cao, J., Zhao, F., & Wan, K. (2022). Seismic constraints on a remnant Mesozoic forearc basin in the northeastern South China Sea. *Gondwana Research*, 102, 77–94. <https://doi.org/10.1016/j.gr.2020.10.006>
- Franke, D., Savva, D., Pubellier, M., Steuer, S., Mouly, B., Auxietre, J.-L., et al. (2014). The final rifting evolution in the South China Sea. *Marine and Petroleum Geology*, 58, 704–720. <https://doi.org/10.1016/j.marpetgeo.2013.11.020>
- Gerbi, C., Culshaw, N., & Marsh, J. (2010). Magnitude of weakening during crustal-scale shear zone development. *Journal of Structural Geology*, 32(1), 107–117. <https://doi.org/10.1016/j.jsg.2009.10.002>
- Gerya, T. (2010). *Introduction to numerical geodynamic modelling*. Cambridge University Press.
- Giambiagi, L. B., Alvarez, P. P., Godoy, E., & Ramos, V. A. (2003). The control of pre-existing extensional structures on the evolution of the southern sector of the Aconagua fold and thrust belt, southern Andes. *Tectonophysics*, 369(1–2), 1–19. [https://doi.org/10.1016/S0040-1951\(03\)00171-9](https://doi.org/10.1016/S0040-1951(03)00171-9)
- Gleason, G. C., & Tullis, J. (1995). A flow law for dislocation creep of quartz aggregates determined with the molten salt cell. *Tectonophysics*, 247(1–4), 1–23. [https://doi.org/10.1016/0040-1951\(95\)00011-B](https://doi.org/10.1016/0040-1951(95)00011-B)
- Glerum, A., Thieulot, C., Fraters, M., Blom, C., & Spakman, W. (2018). Nonlinear viscoplasticity in ASPECT: Benchmarking and applications to subduction. *Solid Earth*, 9(2), 267–294. <https://doi.org/10.5194/se-9-267-2018>
- Guan, W., Huang, L., Liu, C., Peng, G., Li, H., Liang, C., et al. (2023). Interactions between pre-existing structures and rift faults: Implications for basin geometry in the northern South China Sea. *Basin Research*, 36(1), e12822. <https://doi.org/10.1111/bre.12822>
- Hall, R. (2002). Cenozoic geological and plate tectonic evolution of SE Asia and the SW Pacific: Computer-based reconstructions, model and animations. *Journal of Asian Earth Sciences*, 20(4), 353–431. [https://doi.org/10.1016/S1367-9120\(01\)00069-4](https://doi.org/10.1016/S1367-9120(01)00069-4)
- Handy, M. R., & Brun, J. P. (2004). Seismicity, structure and strength of the continental lithosphere. *Earth and Planetary Science Letters*, 223(3–4), 427–441. <https://doi.org/10.1016/j.epsl.2004.04.021>
- Harry, D. L., & Sawyer, D. S. (1992). A dynamic model of extension in the Baltimore Canyon Trough region. *Tectonics*, 11(2), 420–436. <https://doi.org/10.1029/91TC03012>
- Hasterok, D., Gard, M., & Webb, J. (2018). On the radiogenic heat production of metamorphic, igneous, and sedimentary rocks. *Geoscience Frontiers*, 9(6), 1777–1794. <https://doi.org/10.1016/j.gsf.2017.10.012>
- Haxby, W. F., & Turcotte, D. L. (1978). On isostatic geoid anomalies. *Journal of Geophysical Research*, 83(B11), 5473–5478. <https://doi.org/10.1029/JB083iB11p05473>
- Hayes, G. P., Moore, G. L., Portner, D. E., Hearne, M., Flamme, H., Furtney, M., & Smoczyk, G. M. (2018). Slab2, a comprehensive subduction zone geometry model. *Science*, 362(6410), 58–61. <https://doi.org/10.1126/science.aat4723>
- He, Z. Y., & Xu, X. S. (2012). Petrogenesis of the Late Yanshanian mantle-derived intrusions in southeastern China: Response to the geodynamics of paleo-Pacific plate subduction. *Chemical Geology*, 328, 208–221. <https://doi.org/10.1016/j.chemgeo.2011.09.014>
- Heckenbach, E. L., Brune, S., Glerum, A. C., & Bott, J. (2021). Is there a speed limit for the thermal steady-state assumption in continental Rifts? *Geochemistry, Geophysics, Geosystems*, 22(3), e2020GC009577. <https://doi.org/10.1029/2020GC009577>
- Heister, T., Dannberg, J., Gassmüller, R., & Bangerth, W. (2017). High accuracy mantle convection simulation through modern numerical methods—II: Realistic models and problems. *Geophysical Journal International*, 210(2), 833–851. <https://doi.org/10.1093/gji/ggx195>
- Henza, A. A., Withjack, M. O., & Schlische, R. W. (2010). Normal-fault development during two phases of non-coaxial extension: An experimental study. *Journal of Structural Geology*, 32(11), 1656–1667. <https://doi.org/10.1016/j.jsg.2009.07.007>
- Hetzl, R., Passchier, C. W., Ring, U., & Dora, Ö. O. (1995). Bivergent extension in orogenic belts: The Menderes massif (southwestern Turkey). *Geology*, 23(5), 455. [https://doi.org/10.1130/0091-7613\(1995\)023<0455:BEIOBT>2.3.CO;2](https://doi.org/10.1130/0091-7613(1995)023<0455:BEIOBT>2.3.CO;2)
- Hirth, G., & Kohlstedt, D. (2003). Rheology of the upper mantle and the mantle wedge: A view from the experimentalists. *Geophysical Monograph Series*, 138, 83–105. <https://doi.org/10.1029/138gm06>
- Holloway, N. H. (1982). North Palawan block, Philippines—Its relation to Asian Mainland and role in evolution of South China sea. *AAPG Bulletin*, 66. <https://doi.org/10.1306/03B5A7A5-16D1-11D7-8645000102C1865D>
- Hu, J., Tian, Y., Long, Z., Hu, D., Huang, Y., Wang, Y., & Hu, S. (2020). Thermo-rheological structure of the northern margin of the South China Sea: Structural and geodynamic implications. *Tectonophysics*, 777, 228338. <https://doi.org/10.1016/j.tecto.2020.228338>
- Huang, Z.-X., & Xu, Y. (2011). S-wave velocity structure of South China Sea and surrounding regions from surface wave tomography. *Chinese Journal of Geophysics*, 54(6), 978–987. <https://doi.org/10.1002/cjg2.1678>

- Huismans, R. S., & Beaumont, C. (2007). Roles of lithospheric strain softening and heterogeneity in determining the geometry of rifts and continental margins. *Geological Society, London, Special Publications*, 282(1), 111–138. <https://doi.org/10.1144/SP282.6>
- Huismans, R. S., & Beaumont, C. (2014). Rifted continental margins: The case for depth-dependent extension. *Earth and Planetary Science Letters*, 407, 148–162. <https://doi.org/10.1016/j.epsl.2014.09.032>
- Introcaso, A., Pacino, M. C., & Fraga, H. (1992). Gravity, isostasy and Andean crustal shortening between latitudes 30 and 35 S. *Tectonophysics*, 205(1–3), 31–48. [https://doi.org/10.1016/0040-1951\(92\)90416-4](https://doi.org/10.1016/0040-1951(92)90416-4)
- Jadamec, M. A., Turcotte, D. L., & Howell, P. (2007). Analytic models for orogenic collapse. *Tectonophysics*, 435(1–4), 1–12. <https://doi.org/10.1016/j.tecto.2007.01.007>
- Jahn, B.-M., Chen, P. Y., & Yen, T. P. (1976). Rb-Sr ages of granitic rocks in southeastern China and their tectonic significance. *Geological Society of America Bulletin*, 87(5), 763–776. [https://doi.org/10.1130/0016-7606\(1976\)87<763:raogri>2.0.co;2](https://doi.org/10.1130/0016-7606(1976)87<763:raogri>2.0.co;2)
- Jammes, S., & Lavier, L. L. (2019). Effect of contrasting strength from inherited crustal fabrics on the development of rifting margins. *Geosphere*, 15(2), 407–422. <https://doi.org/10.1130/GES01686.1>
- Jolivet, L., Faccenna, C., Huet, B., Labrousse, L., Le Pourhiet, L., Lacombe, O., et al. (2013). Aegean tectonics: Strain localisation, slab tearing and trench retreat. *Tectonophysics*, 597, 1–33. <https://doi.org/10.1016/j.tecto.2012.06.011>
- Jones, C. H., Unruh, J. R., & Sonder, L. J. (1996). The role of gravitational potential energy in active deformation in the southwestern United States. *Nature*, 381(6577), 37–41. <https://doi.org/10.1038/381037a0>
- Keep, M., & McClay, K. R. (1997). Analogue modelling of multiphase rift systems. *Tectonophysics*, 273(3–4), 239–270. [https://doi.org/10.1016/S0040-1951\(96\)00272-7](https://doi.org/10.1016/S0040-1951(96)00272-7)
- Kronbichler, M., Heister, T., & Bangerth, W. (2012). High accuracy mantle convection simulation through modern numerical methods. *Geophysical Journal International*, 191(1), 12–29. <https://doi.org/10.1111/j.1365-246X.2012.05609.x>
- Larsen, H. C., Mohn, G., Nirrengarten, M., Sun, Z., Stock, J., Jian, Z., et al. (2018). Rapid transition from continental breakup to igneous oceanic crust in the South China Sea. *Nature Geoscience*, 11(10), 782–789. <https://doi.org/10.1038/s41561-018-0198-1>
- Lei, C., Alves, T. M., Ren, J., Pang, X., Yang, L., & Liu, J. (2019). Depositional architecture and structural evolution of a region immediately inboard of the locus of continental breakup (Liwan Sub-basin, South China Sea). *GSA Bulletin*, 131(7–8), 1059–1074. <https://doi.org/10.1130/B35001.1>
- Le Pichon, X., & Angelier, J. (1981). The Aegean Sea. *Philosophical Transactions of the Royal Society of London A*, 300, 357–372. <https://doi.org/10.1098/rsta.1981.0071>
- Li, C., Xu, X., Lin, J., Sun, Z., Zhu, J., Yao, Y., et al. (2014). Ages and magnetic structures of the South China Sea constrained by deep tow magnetic surveys and IODP Expedition 349. *Geochemistry, Geophysics, Geosystems*, 15(12), 4958–4983. <https://doi.org/10.1002/2014GC005567>
- Li, F., Sun, Z., & Yang, H. (2018). Possible spatial distribution of the Mesozoic volcanic arc in the present-day South China Sea Continental margin and its tectonic implications. *Journal of Geophysical Research: Solid Earth*, 123(8), 6215–6235. <https://doi.org/10.1029/2017JB014861>
- Li, J., Cawood, P. A., Ratschbacher, L., Zhang, Y., Dong, S., Xin, Y., et al. (2020). Building Southeast China in the late Mesozoic: Insights from alternating episodes of shortening and extension along the Lianhuashan fault zone. *Earth-Science Reviews*, 201, 103056. <https://doi.org/10.1016/j.earscirev.2019.103056>
- Li, K. (2024a). From orogeny to rifting: The role of inherited structures during the formation of the South China Sea (version 1) [Software]. *Zenodo*. <https://doi.org/10.5281/zenodo.12772122>
- Li, K. (2024b). From orogeny to rifting: The role of inherited structures during the formation of the South China Sea (version 1) [Dataset]. *Zenodo*. <https://doi.org/10.5281/zenodo.13942575>
- Li, S., Santosh, M., Zhao, G., Zhang, G., & Jin, C. (2012a). Intracontinental deformation in a frontier of super-convergence: A perspective on the tectonic milieu of the South China Block. *Journal of Asian Earth Sciences*, 49, 313–329. <https://doi.org/10.1016/j.jseae.2011.07.026>
- Li, X., & Zou, H. (2017). Late Cretaceous–Cenozoic exhumation of the southeastern margin of Coastal Mountains, SE China, revealed by fission-track thermochronology: Implications for the topographic evolution. *Solid Earth Sciences*, 2(3), 79–88. <https://doi.org/10.1016/j.sesci.2017.02.001>
- Li, Z. X., & Li, X. H. (2007). Formation of the 1300-km-wide intracontinental orogen and postorogenic magmatic province in Mesozoic South China: A flat-slab subduction model. *Geology*, 35(2), 179. <https://doi.org/10.1130/G23193A.1>
- Li, Z. X., Li, X. H., Chung, S. L., Lo, C. H., Xu, X., & Li, W. X. (2012b). Magmatic switch-on and switch-off along the South China continental margin since the Permian: Transition from an Andean-type to a Western Pacific-type plate boundary. *Tectonophysics*, 532–535, 271–290. <https://doi.org/10.1016/j.tecto.2012.02.011>
- Liu, Z., Dai, L., Li, S., Li, Z. H., Ding, X., Bukhari, S. W. H., & Somerville, I. (2022). Earth's surface responses during geodynamic evolution: Numerical insight from the southern East China Sea Continental Shelf Basin, West Pacific. *Gondwana Research*, 102, 167–179. <https://doi.org/10.1016/j.gr.2020.12.011>
- Lu, B., Wang, P., Wu, J., Li, W., Wang, W., & Lang, Y. (2014). Distribution of the Mesozoic in the continental margin basins of the South China Sea and its petroliferous significance. *Petroleum Exploration and Development*, 41(4), 545–552. [https://doi.org/10.1016/S1876-3804\(14\)60065-3](https://doi.org/10.1016/S1876-3804(14)60065-3)
- Malinverno, A., & Ryan, W. (1986). Extension in the Tyrrhenian Sea and shortening in the Apennines as a result of arc migration driven by sinking of the lithosphere. *Tectonics*, 5(2), 227–245. <https://doi.org/10.1029/TC005i002p00227>
- Manatschal, G., Chenin, P., Lescoutre, R., Miró, J., Cadenas, P., Saspiturry, N., et al. (2021). The role of inheritance in forming rifts and rifted margins and building collisional orogens: A Biscay-Pyrenean perspective. *BSGF - Earth Sciences Bulletin*, 192, 55. <https://doi.org/10.1051/bsgf/2021042>
- Manatschal, G., Lavier, L., & Chenin, P. (2015). The role of inheritance in structuring hyperextended rift systems: Some considerations based on observations and numerical modeling. *Gondwana Research*, 27(1), 140–164. <https://doi.org/10.1016/j.gr.2014.08.006>
- Molnar, N. E., Cruden, A. R., & Betts, P. G. (2019). Interactions between propagating rifts and linear weaknesses in the lower crust. *Geosphere*, 15(5), 1617–1640. <https://doi.org/10.1130/GES02119.1>
- Molnar, P., & Lyon-Caen, H. (1988). Some simple physical aspects of the support, structure, and evolution of mountain belts. *Geological Society of America Special Paper*, 218, 179–208. <https://doi.org/10.1130/SPE218-p179>
- Morley, C. K. (2012). Late cretaceous–early palaeogene tectonic development of SE Asia. *Earth-Science Reviews*, 115(1–2), 37–75. <https://doi.org/10.1016/j.earscirev.2012.08.002>
- Naliboff, J., & Buiter, S. J. (2015). Rift reactivation and migration during multiphase extension. *Earth and Planetary Science Letters*, 421, 58–67. <https://doi.org/10.1016/j.epsl.2015.03.050>

- Naliboff, J. B., Glerum, A., Brune, S., Péron-Pinvidic, G., & Wrona, T. (2020). Development of 3-D rift heterogeneity through fault network evolution. *Geophysical Research Letters*, *47*(13), e2019GL086611. <https://doi.org/10.1029/2019GL086611>
- Neuharth, D., Brune, S., Glerum, A., Morley, C. K., Yuan, X. P., & Braun, J. (2022a). Flexural strike-slip basins. *Geology*, *50*(3), 361–365. <https://doi.org/10.1130/G49351.1>
- Neuharth, D., Brune, S., Wrona, T., Glerum, A., Braun, J., & Yuan, X. P. (2022b). Evolution of rift systems and their fault networks in response to surface processes. *Tectonics*, *41*(3), e2021TC007166. <https://doi.org/10.1029/2021TC007166>
- Oncken, O., Boutelier, D., Dresen, G., & Schemmann, K. (2012). Strain accumulation controls failure of a plate boundary zone: Linking deformation of the Central Andes and lithosphere mechanics. *Geochemistry, Geophysics, Geosystems*, *13*(12), Q12007. <https://doi.org/10.1029/2012GC004280>
- Pérez-Gussinyé, M., Andrés-Martínez, M., Araújo, M., Xin, Y., Armitage, J., & Morgan, J. P. (2020). Lithospheric strength and rift migration controls on synrift stratigraphy and breakup unconformities at rifted margins: Examples from numerical models, the Atlantic and South China Sea margins. *Tectonics*, *39*(12), e2020TC006255. <https://doi.org/10.1029/2020TC006255>
- Peron-Pinvidic, G., Fourel, L., & Buitter, S. J. H. (2022). The influence of orogenic collision inheritance on rifted margin architecture: Insights from comparing numerical experiments to the Mid-Norwegian margin. *Tectonophysics*, *828*, 229273. <https://doi.org/10.1016/j.tecto.2022.229273>
- Peron-Pinvidic, G., Osmundsen, P. T., & Bunkholt, H. (2020). The proximal domain of the Mid-Norwegian rifted margin: The Trøndelag Platform revisited. *Tectonophysics*, *790*, 228551. <https://doi.org/10.1016/j.tecto.2020.228551>
- Persaud, P., Tan, E., Contreras, J., & Lavier, L. (2017). A bottom-driven mechanism for distributed faulting in the Gulf of California rift. *Tectonophysics*, *719–720*, 51–65. <https://doi.org/10.1016/j.tecto.2016.11.024>
- Petersen, K. D., & Schiffer, C. (2016). Wilson cycle passive margins: Control of orogenic inheritance on continental breakup. *Gondwana Research*, *39*, 131–144. <https://doi.org/10.1016/j.gr.2016.06.012>
- Petri, B., Duretz, T., Mohn, G., Schmalholz, S. M., Karner, G. D., & Müntener, O. (2019). Thinning mechanisms of heterogeneous continental lithosphere. *Earth and Planetary Science Letters*, *512*, 147–162. <https://doi.org/10.1016/j.epsl.2019.02.007>
- Phillips, T. B., Jackson, C. A., Bell, R. E., Duffy, O. B., & Fossen, H. (2016). Reactivation of intrabasement structures during rifting: A case study from offshore southern Norway. *Journal of Structural Geology*, *91*, 54–73. <https://doi.org/10.1016/j.jsg.2016.08.008>
- Pysklywec, R. N., & Beaumont, C. (2004). Intraplate tectonics: Feedback between radioactive thermal weakening and crustal deformation driven by mantle lithosphere instabilities. *Earth and Planetary Science Letters*, *221*(1–4), 275–292. [https://doi.org/10.1016/S0012-821X\(04\)00098-6](https://doi.org/10.1016/S0012-821X(04)00098-6)
- Ramos, V. A., Zapata, T., Cristallini, E., & Introcaso, A. (2004). The Andean thrust system latitudinal variations in structural styles and orogenic shortening. *American Association of Petroleum Geologists Memoirs*, *82*, 30–50.
- Richter, M. J., Brune, S., Riedl, S., Glerum, A., Neuharth, D., & Strecker, M. R. (2021). Controls on asymmetric rift dynamics: Numerical modeling of strain localization and fault evolution in the Kenya Rift. *Tectonics*, *40*(5), e2020TC006553. <https://doi.org/10.1029/2020TC006553>
- Riesner, M., Lacassin, R., Simoes, M., Armijo, R., Rauld, R., & Vargas, G. (2017). Kinematics of the active West Andean fold-and-thrust belt (central Chile): Structure and long-term shortening rate: Kinematics of the active West Andean fold-and-thrust belt. *Tectonics*, *36*(2), 287–303. <https://doi.org/10.1002/2016TC004269>
- Rutter, E. H., & Brodie, K. H. (2004). Experimental grain size-sensitive flow of hot-pressed Brazilian quartz aggregates. *Journal of Structural Geology*, *26*(11), 2011–2023. <https://doi.org/10.1016/j.jsg.2004.04.006>
- Rybacki, E., Gottschalk, M., Wirth, R., & Dresen, G. (2006). Influence of water fugacity and activation volume on the flow properties of fine-grained anorthite aggregates. *Journal of Geophysical Research*, *111*(B3), 2005JB003663. <https://doi.org/10.1029/2005JB003663>
- Salazar-Mora, C. A., Huisman, R. S., Fossen, H., & Egydio-Silva, M. (2018). The Wilson cycle and effects of tectonic structural inheritance on rifted passive margin formation. *Tectonics*, *37*(9), 3085–3101. <https://doi.org/10.1029/2018TC004962>
- Savva, D., Pubellier, M., Franke, D., Chamot-Rooke, N., Meresse, F., Steuer, S., & Auxietre, J.-L. (2014). Different expressions of rifting on the South China Sea margins. *Marine and Petroleum Geology*, *58*, 579–598. <https://doi.org/10.1016/j.marpetgeo.2014.05.023>
- Schott, B., & Schmeling, H. (1998). Delamination and detachment of a lithospheric root. *Tectonophysics*, *296*(3–4), 225–247. [https://doi.org/10.1016/S0040-1951\(98\)00154-1](https://doi.org/10.1016/S0040-1951(98)00154-1)
- Sharples, W., Moresi, L.-N., Jadamec, M. A., & Revote, J. (2015). Styles of rifting and fault spacing in numerical models of crustal extension. *Journal of Geophysical Research: Solid Earth*, *120*(6), 4379–4404. <https://doi.org/10.1002/2014JB011813>
- Shi, H., & Li, C. F. (2012). Mesozoic and early Cenozoic tectonic convergence-to-rifting transition prior to opening of the South China Sea. *International Geology Review*, *54*(15), 1801–1828. <https://doi.org/10.1080/00206814.2012.677136>
- Shi, X., Kohn, B., Yu, C., Tian, Y., Li, G., & Zhao, P. (2022). Thermo-tectonic history of coastal NW South China Sea: A low-temperature thermochronology study. *Tectonophysics*, *833*, 229344. <https://doi.org/10.1016/j.tecto.2022.229344>
- Suo, Y., Li, S., Jin, C., Zhang, Y., Zhou, J., Li, X., et al. (2019). Eastward tectonic migration and transition of the Jurassic-Cretaceous Andean-type continental margin along Southeast China. *Earth-Science Reviews*, *196*, 102884. <https://doi.org/10.1016/j.earscirev.2019.102884>
- Tang, Q., & Zheng, C. (2013). Crust and upper mantle structure and its tectonic implications in the South China Sea and adjacent regions. *Journal of Asian Earth Sciences*, *62*, 510–525. <https://doi.org/10.1016/j.jseae.2012.10.037>
- Tapponnier, P., Peltzer, G., & Armijo, R. (1986). On the mechanics of the collision between India and Asia. *Geological Society, London, Special Publications*, *19*(1), 113–157. <https://doi.org/10.1144/GSL.SP.1986.019.01.07>
- Taylor, B., & Hayes, D. E. (1980). The tectonic evolution of the South China Basin. In D. E. Hayes (Ed.), *Geophysical monograph series* (Vol. 23, pp. 89–104). American Geophysical Union. <https://doi.org/10.1029/GM023p0089>
- Taylor, B., & Hayes, D. E. (1983). Origin and history of the South China sea basin. *Washington DC American Geophysical Union Geophysical Monograph Series*, *27*, 23–56. <https://doi.org/10.1029/GM027p0023>
- Tetreault, J. L., & Buitter, S. J. H. (2018). The influence of extension rate and crustal rheology on the evolution of passive margins from rifting to break-up. *Tectonophysics*, *746*, 155–172. <https://doi.org/10.1016/j.tecto.2017.08.029>
- Thomas, W. A. (2006). Tectonic inheritance at a continental margin. *Geological Society of America Today*, *16*(2), 4–11. [https://doi.org/10.1130/1052-5173\(2006\)0162.0.CO;2](https://doi.org/10.1130/1052-5173(2006)0162.0.CO;2)
- Wang, D., & Shu, L. (2012). Late Mesozoic basin and range tectonics and related magmatism in Southeast China. *Geoscience Frontiers*, *3*(2), 109–124. <https://doi.org/10.1016/j.gsf.2011.11.007>
- Wang, J., Pang, X., Liu, B., Zheng, J., & Wang, H. (2018). The Baiyun and Liwan Sags: Two supradetachment basins on the passive continental margin of the northern South China Sea. *Marine and Petroleum Geology*, *95*, 206–218. <https://doi.org/10.1016/j.marpetgeo.2018.05.001>
- Wang, L., Maestrelli, D., Corti, G., Zou, Y., & Shen, C. (2021). Normal fault reactivation during multiphase extension: Analogue models and application to the Turkana depression, East Africa. *Tectonophysics*, *811*, 228870. <https://doi.org/10.1016/j.tecto.2021.228870>

- Wenker, S., & Beaumont, C. (2018). Effects of lateral strength contrasts and inherited heterogeneities on necking and rifting of continents. *Tectonophysics*, 746, 46–63. <https://doi.org/10.1016/j.tecto.2016.10.011>
- Wessel, P., Luis, J. F., Uieda, L. A., Scharroo, R., Wobbe, F., Smith, W. H. F., & Tian, D. (2019). The generic mapping tools version 6. *Geochemistry, Geophysics, Geosystems*, 20(11), 5556–5564. <https://doi.org/10.1029/2019GC008515>
- Wie, X. D., Ruan, A. G., Zhao, M. H., Qiu, X. L., Li, J. B., Zhu, J. J., et al. (2011). A wide-angle obs profile across the dongsha uplift and chaoshan depression in the mid-northern South China Sea. *Chinese Journal of Geophysics*, 54(6), 1149–1160. <https://doi.org/10.1002/cjg2.1691>
- Wilson, J. T. (1966). Did the Atlantic close and then re-open? *Nature*, 211(5050), 676–681. <https://doi.org/10.1038/211676a0>
- Wilson, R. W., Houseman, G. A., Buiter, S. J. H., McCaffrey, K. J., & Doré, A. G. (2019). Fifty years of the Wilson Cycle concept in plate tectonics: An overview. *Geological Society, London, Special Publications*, 470(1), 1–17. <https://doi.org/10.1144/SP470-2019-58>
- Xia, G., Yi, H., Zhao, X., Gong, D., & Ji, C. (2012). A late Mesozoic high plateau in eastern China: Evidence from basalt vesicular paleoaltimetry. *Chinese Science Bulletin*, 57(21), 2767–2777. <https://doi.org/10.1007/s11434-012-5169-0>
- Xu, C., Shi, H., Barnes, C. G., & Zhou, Z. (2016). Tracing a late Mesozoic magmatic arc along the Southeast Asian margin from the granitoids drilled from the northern South China Sea. *International Geology Review*, 58(1), 71–94. <https://doi.org/10.1080/00206814.2015.1056256>
- Yan, P., Wang, L., & Wang, Y. (2014). Late Mesozoic compressional folds in Dongsha waters, the northern margin of the South China Sea. *Tectonophysics*, 615–616, 213–223. <https://doi.org/10.1016/j.tecto.2014.01.009>
- Yan, P., Zhou, D., & Liu, Z. L. (2001). A crustal structure profile across the northern continental margin of the South China Sea. *Tectonophysics*, 338(1), 1–21. [https://doi.org/10.1016/S0040-1951\(01\)00062-2](https://doi.org/10.1016/S0040-1951(01)00062-2)
- Yang, L., Ren, J., McIntosh, K., Pang, X., Lei, C., & Zhao, Y. (2018). The structure and evolution of deepwater basins in the distal margin of the northern South China Sea and their implications for the formation of the continental margin. *Marine and Petroleum Geology*, 92, 234–254. <https://doi.org/10.1016/j.marpetgeo.2018.02.032>
- Ye, Q., Mei, L., Shi, H., Camanni, G., Shu, Y., Wu, J., et al. (2018). The Late Cretaceous tectonic evolution of the South China Sea area: An overview, and new perspectives from 3D seismic reflection data. *Earth-Science Reviews*, 187, 186–204. <https://doi.org/10.1016/j.earscirev.2018.09.013>
- Ye, Q., Mei, L., Shi, H., Du, J., Deng, P., Shu, Y., & Camanni, G. (2020). The influence of pre-existing basement faults on the Cenozoic structure and evolution of the proximal domain, northern South China Sea rifted margin. *Tectonics*, 39(3), e2019TC005845. <https://doi.org/10.1029/2019TC005845>
- Yuan, X. P., Braun, J., Guerit, L., Rouby, D., & Cordonnier, G. (2019a). A new efficient method to solve the stream power law model taking into account sediment deposition. *Journal of Geophysical Research: Earth Surface*, 124(6), 1346–1365. <https://doi.org/10.1029/2018JF004867>
- Yuan, X. P., Braun, J., Guerit, L., Simon, B., Bovy, B., Rouby, D., et al. (2019b). Linking continental erosion to marine sediment transport and deposition: A new implicit and O (N) method for inverse analysis. *Earth and Planetary Science Letters*, 524, 115728. <https://doi.org/10.1016/j.epsl.2019.115728>
- Zahirovic, S., Seton, M., & Müller, R. D. (2014). The cretaceous and Cenozoic tectonic evolution of southeast Asia. *Solid Earth*, 5(1), 227–273. <https://doi.org/10.5194/se-5-227-2014>
- Zhang, C., Manatschal, G., Pang, X., Sun, Z., Zheng, J., Li, H., et al. (2020). Discovery of Mega-Sheath Folds Flooring the Liwan Subbasin (South China Sea): Implications for the Rheology of Hyperextended Crust. *Geochemistry, Geophysics, Geosystems*, 21(7), e2020GC009023. <https://doi.org/10.1029/2020GC009023>
- Zhao, Y., Ren, J., Pang, X., Yang, L., & Zheng, J. (2018). Structural style, formation of low angle normal fault and its controls on the evolution of Baiyun Rift, northern margin of the South China Sea. *Marine and Petroleum Geology*, 89, 687–700. <https://doi.org/10.1016/j.marpetgeo.2017.11.001>
- Zhou, D., Sun, Z., Chen, H., Xu, H., Wang, W., Pang, X., et al. (2008). Mesozoic paleogeography and tectonic evolution of South China Sea and adjacent areas in the context of Tethyan and Paleo-Pacific interconnections. *Island Arc*, 17(2), 186–207. <https://doi.org/10.1111/j.1440-1738.2008.00611.x>
- Zhou, X., Sun, T., Shen, W., Shu, L., & Niu, Y. (2006). Petrogenesis of Mesozoic granitoids and volcanic rocks in South China: A response to tectonic evolution. *Episodes*, 29(1), 26–33. <https://doi.org/10.18814/epiiugs/2006/v29i1/004>
- Zhou, X. M., & Li, W. X. (2000). Origin of Late Mesozoic igneous rocks in Southeastern China: Implications for lithosphere subduction and underplating of mafic magmas. *Tectonophysics*, 326(3–4), 269–287. [https://doi.org/10.1016/S0040-1951\(00\)00120-7](https://doi.org/10.1016/S0040-1951(00)00120-7)
- Zoback, M. L., & Mooney, W. D. (2003). Lithospheric buoyancy and continental intraplate stresses. *International Geology Review*, 45(2), 95–118. <https://doi.org/10.2747/0020-6814.45.2.95>